Crustal-scale reflection imaging and interpretation by passive seismic interferometry using local earthquakes

Yohei Nishitsuji[1], Shohei Minato[1], Boris Boullenger[1], Martín Gomez[2], Kees Wapenaar[1], and Deyan Draganov[1]

Abstract

We have developed an application of passive seismic interferometry (SI) using P-wave coda of local earthquakes for the purpose of crustal-scale reflection imaging. We processed the reflection gathers retrieved from SI following a standard seismic processing in exploration seismology. We applied SI to the P-wave coda using crosscorrelation, crosscoherence, and multidimensional deconvolution (MDD) approaches for data recorded in the Malargüe region, Argentina. Comparing the results from the three approaches, we found that MDD based on the truncated singular-value decomposition scheme gave us substantially better structural imaging. Although our results provided higher resolution images of the subsurface, they showed less clear images for the Moho in comparison with previous seismic images in the region obtained by the receiver function and global-phase SI. Above the Moho, we interpreted a deep thrust fault and the possible melting zones, which were previously indicated by active-seismic and magnetotelluric methods in this region, respectively. The method we developed could be an alternative option not only for crustal-scale imaging, e.g., in enhanced geothermal systems, but also for lithospheric-scale as well as basin-scale imaging, depending on the availability of local earthquakes and the frequency bandwidth of their P-wave coda.

Introduction

Crustal imaging is vitally relevant for understanding processes such as earthquake mechanisms, magmatism, deep geothermal explorations, and basin tectonics. To obtain an image of the crust, active sources (e.g., vibroseis and airguns) and passive sources (e.g., ambient noise and earthquakes) have been used. For the former, the reflection (e.g., Granath et al., 2010) and refraction methods (e.g., Zhao et al., 2013) are well-known, whereas for the latter, traveltime tomography (Aki et al., 1977), full-waveform tomography (Operto et al., 2006), the receiver function (Langston, 1979), and Sp-wave method (Doi and Kawakata, 2013) have been applied.

A very attractive passive seismic method is seismic interferometry (SI) (e.g., Aki, 1957; Claerbout, 1968; Campillo and Paul, 2003; Shapiro and Campillo, 2004; Wapenaar, 2004), which retrieves virtual seismic records from existing seismic records. In this study, we focus on body-wave SI. Although the imaging resolution achieved by passive SI might not be easily compatible with the one achieved by the active-source reflection method, it has the potential to contain low-frequency information, i.e., ≤ 5 Hz, which enables us to interpret deeper structures, such as in the lower crust and lithosphere. Moreover, as an economically attractive aspect, the shooting cost of the passive seismic method is zero. For reflection retrieval by passive SI, several applications have been already reported, for ambient noise (e.g., Draganov et al., 2009; Zhan et al., 2010; Ryberg, 2011; Almagro Vidal et al., 2014; Panea et al., 2014) and local earthquakes (e.g., Nakata et al., 2011, 2014).

There are five ways SI can be applied: using correlation (Claerbout, 1968; Duvall et al., 1993), coherence (Aki, 1957), trace deconvolution (Snieder and Şafak, 2006; Vasconcelos and Snieder, 2008a, 2008b), convolution (Slob et al., 2007), and multidimensional deconvolution (MDD) (Wapenaar et al., 2008). Nakata et al. (2011) compare the common-midpoint (CMP) stacks obtained from SI by crosscorrelation, trace deconvolution, and crosscoherence using traffic noise. The authors suggested that the selection of a proper SI method depends on the data set at hand. In addition to the synthetic comparison of the results obtained from crosscorrelation and MDD by Wapenaar et al. (2011), Nakata et al. (2014) compare SI results obtained using trace deconvolution, crosscoherence, and MDD results (after applying wavefield decomposition), apply

[1]Delft University of Technology, Department of Geoscience and Engineering, Delft, The Netherlands. E-mail: y.nishitsuji@tudelft.nl; s.minato-1@tudelft.nl; b.boullenger@tudelft.nl; c.p.a.wapenaar@tudelft.nl; d.s.draganov@tudelft.nl.
[2]International Center for Earth Sciences, Comision Nacional de Energia Atomica, Buenos Aires, Argentina. E-mail: mpgomezfw@gmail.com.
Manuscript received by the Editor 30 December 2015; revised manuscript received 23 March 2016; published online 8 June 2016. This paper appears in *Interpretation*, Vol. 4, No. 3 (August 2016); p. SJ29–SJ53, 18 FIGS., 1 TABLE.
http://dx.doi.org/10.1190/INT-2015-0226.1.

to data representing local earthquakes to retrieve reflected plane waves. They conclude that MDD provides gathers that have the best signal-to-noise ratio (S/N) among the compared SI methods.

In this paper, we propose a seismic imaging technique that applies passive SI (two-way traveltime ≤ 20 s) to P-wave coda due to local earthquakes ($2^\circ \leq$ epicentral distances $\leq 6^\circ$). Hereafter, we abbreviate this method as local-earthquake P-wave coda (LEPC) SI. The coda waves are the tail part of a signal consisting of multiply scattered waves (Snieder, 2004). Hence, we assume that their directivity is weak (e.g., Mayeda et al., 2007; Baltay et al., 2010; Abercrombie, 2012), and thus that they illuminate the subsurface beneath the receivers favorably for retrieval of reflections. We apply LEPC SI to data recorded by an exploration-type receiver array called MalARRgue (Ruigrok et al., 2012) that was located in the Malargüe region (Mendoza, Argentina; Figure 1). Because the west coast of Chile has considerable seismicity due to the Nazca-slab subduction, we choose this region to test LEPC SI.

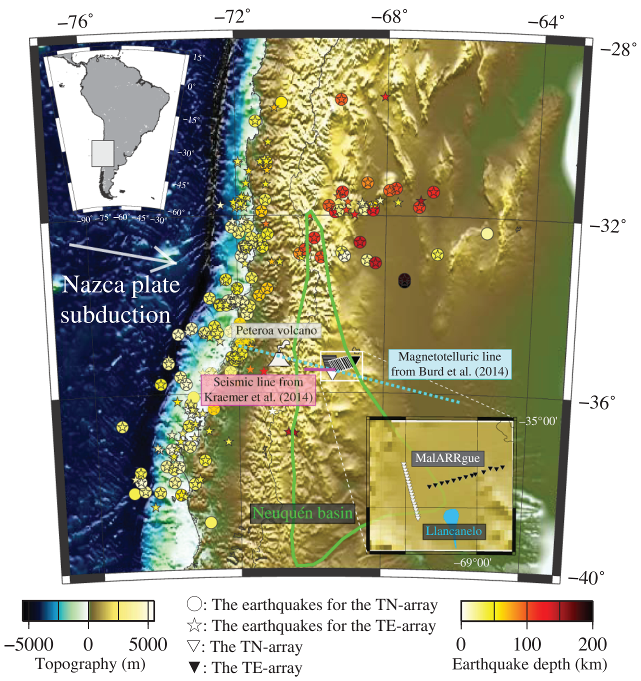

Figure 1. Distribution map of the local earthquakes ($2^\circ \leq$ epicentral distance $\leq 6^\circ$) used in our study. The 115 circles and 210 stars show the locations of the earthquakes recorded by the TN- (the white triangles) and TE-array (black triangles) parts of the MalARRgue array; the earthquakes are color scaled as a function of their focal depth. The volcano symbol indicates the location of the Peteroa volcano. The green outline indicates an approximated location of the Neuquén basin (derived from Mescua et al., 2013). The blue polygon indicates an approximated location of Llancanelo Lake. The solid magenta and dashed blue lines indicate the location at which active-source seismic and the magnetotelluric sections are obtained by Kraemer et al. (2011) and Burd et al. (2014), respectively, which are discussed in the "Results and interpretation" section of this paper.

In the following, we show how to apply LEPC SI using the different retrieval methods (crosscorrelation, crosscoherence, and MDD) for the purpose of crustal-scale reflection imaging.

Study area and data

The Malargüe region is located in the northern part of the Neuquén basin, Argentina. This basin has been producing nearly half of the Argentine hydrocarbons, but has also been providing geothermal power. The Peteroa volcano, which is an active volcano in the Andes Mountains in the Malargüe region, is situated close to part of the array we use (Figure 1). The locations of local earthquakes that occurred in 2012 around the Malargüe region are shown in Figure 1 on a topography map (Becker et al., 2009). The source locations of the earthquakes are provided by Java version of Windows Extracted from Event Data (JWEED) operated by the Incorporated Research Institutions for Seismology (IRIS). We define local earthquakes as those earthquakes, whose epicentral distances are between 2° and 6°. This definition is close to the one introduced by Kayal (2008). For the sake of terminological clarification, regional earthquakes, which we do not use in this study, are the earthquakes whose epicentral distances are larger than 6°. In Figure 1, we indicate with triangles the location of the part of the MalARRgue that we use in our study: the T-array, which is a linear receiver array deployed at the surface. The T-array consists of two linear subarrays: the TN-array with 19 stations spaced every 2 km (labeled TN02 to TN20; white triangles in Figure 1), oriented in the north-northwest direction; and the TE-array with 13 stations spaced every 4 km (labeled TE01 to TE13; black triangles in Figure 1), oriented in the east-northeast direction. These stations are 3C velocity sensors. The 115 circles and 210 stars indicate the location of the local earthquakes recorded by the TN- and TE-arrays, respectively, and characterized by sufficient S/N of the P-wave coda. The TE-array recorded a higher number of earthquakes than the TN-array, because the TE-array was operating longer. The coverage of back azimuth of these earthquakes with respect to the T-array is wide (Figures 1 and 2). A complete list of the local earthquakes used in this study is shown in Table 1.

Local-earthquake P-wave coda seismic interferometry

Crosscorrelation

In Claerbout (1968), virtual reflection traces were retrieved from the autocorrelation of the recorded transmission response in a horizontally layered medium. Later, he conjectures that in 3D inhomogeneous media, one has to use crosscorrelation to retrieve the reflection response between two receivers at the surface. This is proven by Wapenaar (2004) for an arbitrary inhomogeneous elastic medium. The author shows that the Green's function $G^{v,t}_{p,q}(\mathbf{x}_A, \mathbf{x}_B, \omega)$, representing particle-velocity measurement v in the p-direction at a receiver

Table 1. Local earthquakes used in this study.

Date (month/day/year)	Time (h:min:s)	Latitude (°N)	Longitude (°E)	Depth (km)	M_b	Array ID
01/17/2012	15:09:02	−30.814	−71.214	75	3.9	TE
01/17/2012	23:21:34	−31.605	−71.686	31	5.5	TE
01/18/2012	3:17:16	−31.589	−71.789	50	4.7	TE
01/18/2012	11:33:03	−31.798	−68.397	10	4.6	TE
01/18/2012	11:35:52	−31.665	−68.164	19	5.0	TE
01/19/2012	3:58:17	−31.756	−68.657	15	4.6	TE
01/19/2012	7:10:20	−31.635	−71.898	38	4.9	TE
01/19/2012	8:22:49	−32.193	−71.213	87	3.9	TE
01/20/2012	5:26:33	−31.273	−71.736	49	3.4	TE
01/20/2012	6:05:41	−31.982	−68.843	117	3.5	TE
01/23/2012	16:04:53	−36.455	−73.182	24	5.8	TE
01/23/2012	16:29:30	−36.380	−73.267	25	4.0	TE
01/23/2012	16:30:55	−36.457	−73.023	25	3.9	TE
01/23/2012	17:22:06	−36.344	−73.443	4	5.0	TE
01/23/2012	17:53:45	−36.472	−73.365	6	4.4	TE
01/23/2012	21:55:15	−36.364	−73.304	28	5.0	TE
01/24/2012	1:45:28	−34.525	−71.949	40	4.5	TE
01/24/2012	16:08:48	−31.651	−67.078	150	3.7	TE
01/24/2012	17:07:49	−31.760	−72.416	9	4.6	TE
01/26/2012	2:23:10	−29.325	−68.081	118	3.6	TE
01/26/2012	4:57:07	−34.831	−72.498	19	3.9	TE
01/27/2012	2:24:10	−34.708	−71.824	17	4.1	TE
01/31/2012	13:08:00	−33.817	−72.135	12	4.6	TE
01/31/2012	19:40:03	−33.876	−71.997	18	4.0	TE
01/31/2012	21:24:05	−32.788	−71.712	39	3.3	TE
02/01/2012	2:43:19	−32.678	−71.336	52	4.8	TE
02/01/2012	2:43:25	−32.950	−70.256	40	4.7	TE
02/01/2012	2:43:27	−33.053	−70.851	44	4.7	TE
02/04/2012	10:12:55	−38.551	−74.433	35	4.2	TE
02/05/2012	3:42:08	−36.690	−73.243	38	4.7	TE
02/07/2012	12:02:11	−37.902	−74.974	18	4.9	TE
02/10/2012	2:05:22	−30.791	−71.304	57	4.9	TE
02/10/2012	4:07:51	−30.735	−71.222	38	3.8	TE
02/11/2012	2:58:17	−37.456	−73.884	20	5.6	TE
02/11/2012	8:41:14	−36.851	−72.860	40	4.0	TE
02/14/2012	5:58:02	−32.010	−70.034	103	4.5	TE
02/14/2012	8:19:27	−34.948	−71.684	52	4.5	TE
02/15/2012	7:36:14	−34.665	−72.958	10	4.4	TE
02/15/2012	14:08:47	−35.209	−73.926	19	4.7	TE
02/16/2012	22:01:46	−37.255	−74.245	5	4.2	TE
02/17/2012	8:01:14	−37.208	−74.313	17	4.8	TE
02/17/2012	8:01:19	−37.175	−73.646	14	4.8	TE
02/17/2012	19:11:23	−37.233	−73.785	35	4.3	TE
02/18/2012	2:06:27	−34.547	−72.098	29	4.5	TE
02/18/2012	3:50:49	−37.104	−72.316	35	4.0	TE
02/18/2012	17:44:48	−32.097	−71.771	18	4.9	TE
02/22/2012	15:03:39	−33.089	−71.785	33	4.5	TE
02/22/2012	22:38:40	−34.765	−71.809	47	4.0	TE
03/01/2012	6:44:27	−38.331	−73.585	35	4.2	TE

Table 1. Local earthquakes used in this study. (continued)

Date (month/day/year)	Time (h:min:s)	Latitude (°N)	Longitude (°E)	Depth (km)	M_b	Array ID
03/01/2012	18:41:47	−31.572	−69.273	96	4.6	TE
03/03/2012	11:01:47	−30.348	−71.129	49	5.5	TE
03/03/2012	22:12:55	−35.749	−72.800	13	4.9	TE
03/03/2012	22:45:40	−35.731	−72.966	10	4.7	TE
03/03/2012	23:41:30	−35.528	−72.726	28	4.6	TE
03/03/2012	23:43:04	−35.740	−72.975	10	4.9	TE
03/09/2012	0:43:36	−34.730	−72.781	39	4.3	TE
03/12/2012	19:37:36	−34.969	−71.664	70	4.9	TE
03/16/2012	6:20:12	−36.895	−73.596	27	4.7	TE
03/16/2012	23:31:54	−33.606	−72.038	46	4.7	TE
03/17/2012	1:36:00	−33.480	−72.372	21	4.0	TE
03/21/2012	2:41:00	−35.789	−72.029	67	4.6	TE
03/23/2012	9:25:32	−31.691	−69.025	95	4.3	TE
03/24/2012	7:28:33	−33.052	−71.063	69	5.0	TE
03/25/2012	22:37:06	−35.200	−72.217	41	6.5	TE
03/26/2012	2:07:41	−34.994	−72.092	35	4.4	TE
03/27/2012	2:46:12	−37.002	−73.275	23	4.5	TE
03/28/2012	3:23:39	−35.541	−72.998	16	4.7	TE
03/30/2012	7:12:52	−35.196	−72.187	38	4.5	TE/TN
03/31/2012	21:52:56	−35.267	−72.089	43	4.4	TE/TN
04/01/2012	19:09:57	−31.908	−71.322	65	4.9	TE/TN
04/03/2012	2:11:03	−33.847	−72.757	32	5.0	TE/TN
04/06/2012	1:30:12	−34.766	−71.608	37	3.7	TE
04/06/2012	13:25:05	−38.226	−75.019	35	4.9	TN
04/06/2012	17:11:27	−36.926	−73.899	10	4.7	TE
04/06/2012	21:04:54	−35.598	−72.834	13	4.1	TE/TN
04/07/2012	19:13:29	−37.408	−73.870	44	4.4	TE
04/13/2012	6:13:16	−35.210	−72.020	40	4.7	TE/TN
04/15/2012	18:58:21	−32.385	−71.940	27	4.4	TE/TN
04/16/2012	10:34:14	−36.241	−73.352	27	4.3	TE/TN
04/17/2012	3:50:16	−32.625	−71.365	29	6.2	TE/TN
04/17/2012	4:03:18	−32.553	−71.366	40	4.9	TE/TN
04/17/2012	17:53:57	−33.998	−72.342	11	4.1	TE/TN
04/17/2012	23:37:36	−32.617	−71.591	25	3.5	TE/TN
04/19/2012	1:14:06	−30.868	−71.188	65	4.7	TE/TN
04/21/2012	5:14:37	−36.354	−72.709	63	4.0	TE/TN
04/21/2012	22:18:11	−38.224	−74.289	31	4.7	TE/TN
04/27/2012	17:58:24	−35.121	−71.901	43	4.7	TE/TN
04/27/2012	18:34:38	−34.722	−71.721	43	4.7	TE/TN
04/28/2012	20:46:48	−32.653	−71.829	5	4.1	TE
04/30/2012	7:39:46	−29.868	−71.460	37	5.6	TE/TN
05/01/2012	2:43:34	−29.456	−70.770	57	4.6	TN
05/01/2012	20:52:14	−30.813	−71.935	22	4.8	TE
05/05/2012	23:06:53	−31.474	−69.173	110	4.3	TE/TN
05/10/2012	17:11:52	−37.249	−73.914	10	4.4	TE/TN
05/11/2012	19:41:21	−32.901	−71.878	13	4.3	TE/TN
05/12/2012	5:27:36	−34.896	−71.864	44	4.0	TE/TN
05/12/2012	18:15:09	−34.523	−73.269	15	4.7	TE/TN
05/13/2012	12:42:50	−32.740	−71.799	12	4.8	TE/TN
05/16/2012	9:02:01	−36.901	−70.623	144	4.3	TE

Table 1. Local earthquakes used in this study. (continued)

Date (month/day/year)	Time (h:min:s)	Latitude (°N)	Longitude (°E)	Depth (km)	M_b	Array ID
05/16/2012	10:15:36	−35.528	−71.312	118	4.3	TE
05/17/2012	2:34:14	−31.777	−69.530	97	4.4	TE/TN
05/17/2012	6:50:54	−32.697	−71.816	29	4.6	TE/TN
05/18/2012	10:33:12	−31.807	−68.348	60	4.4	TE/TN
05/20/2012	3:32:00	−30.782	−71.353	48	3.8	TE
05/21/2012	5:15:26	−31.263	−68.507	84	4.3	TE/TN
05/21/2012	11:13:33	−30.994	−71.648	59	4.4	TE
05/22/2012	6:22:01	−32.244	−71.691	31	4.3	TE/TN
05/24/2012	19:18:55	−36.912	−70.467	150	5.1	TE
05/31/2012	8:27:17	−34.225	−71.751	20	4.5	TE/TN
06/01/2012	18:19:52	−31.718	−68.635	19	4.7	TE
06/02/2012	21:36:12	−36.174	−73.725	56	4.1	TE
06/07/2012	7:40:54	−31.643	−71.219	36	4.7	TE/TN
06/11/2012	9:50:59	−37.072	−73.661	40	4.2	TE
06/15/2012	5:43:13	−38.188	−74.702	22	4.7	TE/TN
06/18/2012	7:46:23	−36.692	−75.280	30	4.2	TE/TN
06/18/2012	8:29:04	−33.009	−68.496	23	5.3	TE/TN
06/21/2012	9:24:22	−35.523	−72.223	28	4.5	TE/TN
06/23/2012	6:39:32	−34.563	−71.919	47	4.2	TE/TN
06/23/2012	18:14:21	−31.580	−71.856	42	4.7	TE
06/25/2012	13:38:17	−37.970	−74.821	10	4.6	TE/TN
06/26/2012	7:09:27	−35.473	−71.676	84	4.5	TE
06/26/2012	17:01:37	−37.758	−74.820	35	4.6	TE/TN
06/27/2012	13:06:34	−31.701	−67.692	41	4.5	TE
06/27/2012	22:04:25	−32.676	−71.722	20	3.9	TE/TN
06/28/2012	10:33:17	−36.085	−73.270	30	4.3	TN
06/28/2012	11:49:11	−31.447	−66.754	116	4.6	TE/TN
07/04/2012	8:33:05	−38.040	−73.288	33	4.7	TE/TN
07/04/2012	22:57:16	−37.631	−74.077	21	4.6	TE/TN
07/05/2012	5:53:00	−34.494	−72.638	39	3.9	TE/TN
07/07/2012	10:52:15	−32.502	−71.600	33	4.8	TE/TN
07/09/2012	1:44:27	−35.213	−72.069	50	4.5	TE/TN
07/09/2012	12:56:37	−33.061	−68.263	142	4.6	TE/TN
07/09/2012	14:24:37	−37.700	−73.870	30	4.3	TE/TN
07/15/2012	8:23:25	−33.483	−67.477	200	4.6	TE/TN
07/17/2012	22:03:26	−31.298	−71.210	52	4.0	TE
07/30/2012	18:49:45	−35.771	−74.163	44	4.8	TE/TN
08/02/2012	15:01:32	−31.862	−68.575	20	4.3	TE/TN
08/04/2012	13:11:46	−32.835	−69.175	33	4.3	TE/TN
08/04/2012	19:05:39	−31.928	−69.358	119	5.0	TE/TN
08/17/2012	20:19:54	−35.613	−73.615	20	4.7	TE/TN
08/23/2012	19:03:48	−35.776	−73.462	11	4.8	TE/TN
08/24/2012	22:30:01	−33.434	−72.310	42	4.7	TE/TN
08/27/2012	1:29:45	−31.386	−67.746	105	4.2	TE/TN
08/27/2012	4:17:56	−34.709	−71.762	55	4.0	TE/TN
08/28/2012	8:11:25	−32.418	−71.169	44	4.8	TE/TN
08/30/2012	8:04:40	−37.199	−73.397	23	5.0	TE/TN
09/04/2012	5:30:17	−32.516	−69.916	112	4.5	TE/TN
09/06/2012	18:58:03	−36.719	−73.408	35	4.7	TE/TN
09/11/2012	6:35:38	−31.875	−68.350	124	5.1	TE/TN

Table 1. Local earthquakes used in this study. (continued)

Date (month/day/year)	Time (h:min:s)	Latitude (°N)	Longitude (°E)	Depth (km)	M_b	Array ID
09/11/2012	7:24:37	−38.001	−73.860	21	4.6	TE/TN
09/12/2012	9:20:58	−32.606	−68.692	139	4.6	TE/TN
09/15/2012	0:40:16	−34.638	−72.564	34	4.7	TE/TN
09/15/2012	0:50:45	−34.622	−72.923	26	4.5	TE/TN
09/15/2012	9:37:18	−32.853	−66.601	36	4.6	TE/TN
09/18/2012	3:53:30	−31.893	−69.262	26	4.4	TE/TN
09/20/2012	10:07:07	−34.436	−71.951	60	4.5	TE/TN
09/21/2012	9:22:26	−32.947	−69.739	101	4.4	TE/TN
09/28/2012	3:11:50	−31.430	−67.915	96	4.1	TE/TN
09/28/2012	19:21:47	−34.603	−73.369	10	4.3	TE
10/01/2012	8:06:29	−30.786	−71.184	56	4.6	TE/TN
10/05/2012	8:44:51	−34.899	−71.937	60	4.4	TE/TN
10/06/2012	3:18:15	−32.132	−72.107	9	4.6	TE
10/06/2012	22:49:38	−32.127	−71.860	7	4.3	TE
10/08/2012	13:03:42	−34.654	−73.639	14	4.2	TE/TN
10/09/2012	3:30:33	−29.393	−69.211	97	4.8	TE/TN
10/10/2012	18:05:02	−34.039	−71.675	33	4.1	TE/TN
10/11/2012	2:38:30	−34.000	−72.500	32	4.6	TE/TN
10/11/2012	4:38:24	−33.996	−72.442	35	4.7	TE/TN
10/11/2012	17:22:10	−32.865	−70.310	82	5.5	TE/TN
10/11/2012	21:36:08	−34.011	−72.483	43	4.2	TE/TN
10/14/2012	3:37:30	−34.606	−72.209	15	4.5	TE/TN
10/14/2012	10:50:17	−35.310	−73.932	21	4.8	TE/TN
10/15/2012	21:04:21	−31.814	−71.787	24	5.2	TE
10/18/2012	4:38:00	−31.827	−72.034	29	4.5	TE
10/18/2012	5:23:14	−34.689	−71.906	43	4.2	TE/TN
10/19/2012	5:35:22	−31.793	−72.024	43	3.8	TE
10/19/2012	22:48:18	−31.758	−71.950	10	4.6	TE
10/20/2012	0:25:48	−32.251	−72.141	22	4.4	TE/TN
10/21/2012	11:40:36	−37.658	−73.723	15	4.5	TE/TN
10/24/2012	3:46:30	−31.698	−72.069	44	4.7	TE
10/25/2012	5:37:58	−32.773	−70.165	105	4.8	TE/TN
10/25/2012	19:25:41	−29.568	−70.968	69	4.1	TE
10/27/2012	12:33:05	−33.642	−72.006	47	4.4	TE/TN
10/28/2012	1:43:00	−33.404	−71.608	34	3.9	TE/TN
11/01/2012	23:43:38	−31.794	−67.119	109	4.3	TE/TN
11/02/2012	23:42:36	−34.848	−71.789	60	4.5	TE/TN
11/04/2012	14:33:06	−31.729	−71.885	43	4.2	TE/TN
11/07/2012	15:16:27	−30.780	−71.934	34	4.6	TE
11/07/2012	18:37:50	−37.948	−73.141	38	4.4	TE
11/07/2012	22:41:33	−37.512	−72.985	39	4.8	TE/TN
11/08/2012	6:24:10	−32.710	−71.310	46	4.3	TE/TN
11/08/2012	23:57:57	−31.882	−69.070	107	4.6	TE
11/09/2012	6:31:44	−33.427	−67.479	187	4.1	TE/TN
11/11/2012	5:10:56	−33.962	−72.132	13	4.6	TE/TN
11/11/2012	5:46:48	−33.977	−72.183	16	4.8	TE/TN
11/11/2012	7:24:21	−33.973	−72.272	38	4.4	TE/TN
11/15/2012	20:32:37	−32.666	−71.825	23	4.7	TE
11/15/2012	23:41:02	−30.988	−71.171	66	4.2	TE
11/17/2012	23:51:39	−37.594	−73.825	21	4.0	TE

at $\mathbf{x}_A$ due to a point single-force t at $\mathbf{x}_B$ in the q-direction, can be retrieved from the crosscorrelation of observed particle-velocity measurements v_p^{obs} and v_q^{obs} at $\mathbf{x}_A$ and $\mathbf{x}_B$, respectively, from uncorrelated noise sources in the subsurface

$$2Re\{G_{p,q}^{v,t}(\mathbf{x}_A, \mathbf{x}_B, \omega)\}S_N(\omega) \approx -\langle\{v_p^{\mathrm{obs}}(\mathbf{x}_A, \omega)\}^*\{v_q^{\mathrm{obs}}(\mathbf{x}_B, \omega)\}\rangle. \quad (1)$$

The above equation is written in the frequency domain, indicated by the angular frequency ω; the asterisk denotes complex conjugation; $\langle\rangle$ indicates averaging over source realizations; and the particle-velocity measurements are in the p- and q-directions. The observed data v^{obs} is representing the superposition of recordings from uncorrelated noise sources distributed along a surface that illuminated the received from all directions. The value $S_N(\omega)$ denotes the power spectrum of the noise. Due to the source-receiver configuration in this study, we exclude the direct wave, which would not fall inside the stationary-phase region for retrieval of reflections. This happens because the epicentral distances of the earthquakes are relatively long compared with their hypocentral depth. We thus aim to use arrivals characterized by slowness smaller than the ones characterizing the direct waves. Note that the exclusion of the direct waves might give rise to artifacts in the retrieved response. Nevertheless, these artifacts should not pose a problem as long as our main aim is to recover the primary reflections. Moreover, having sufficiently long recordings of coda waves would ensure illumination of the receivers from all directions due to equipartitioning. In such a case, one can exchange the noise recordings in equation 1 by recordings of coda waves v^c. For our application, we define an observed P-wave coda of a local earthquake as

$$v_z^c(\mathbf{x}_A, \omega) = G_z^c(\mathbf{x}_A, \mathbf{x}_S, \omega)E(\mathbf{x}_S, \omega), \quad (2)$$

where z indicates that we are using the vertical component of the recordings and $E(\mathbf{x}_S, \omega)$ is the Fourier transform of the source time function (STF) of a local earthquake at $\mathbf{x}_S$ in the subsurface. As P-wave coda, we use the part of the recording after the direct arrival of the P-phase and before the direct arrival of the S-phase.

Because of the limitation on the length of the coda recordings, we cannot expect that the receivers would be illuminated equally well from all directions. Because of this, we would like to repeat the correlation for many local earthquakes with wide distribution of the back azimuth (Figures 1 and 2) and to average the separate correlations. Thus, we rewrite equation 1 as

$$2Re\{G_{z,z}^{v,t}(\mathbf{x}_A, \mathbf{x}_B, \omega)\}\bar{S}_E(\omega) \propto -\sum_{S=1}^{n}[\{v_z^c(\mathbf{x}_A, \omega)\}^* v_z^c(\mathbf{x}_B, \omega)], \quad (3)$$

where we have exchanged $\langle\rangle$ of equation 1 by a summation over the independent local earthquakes. $\bar{S}_E(\omega)$ denotes the average power spectrum of the STF over the earthquakes.

Crosscoherence

The crosscoherence method (Aki, 1957) is a technique to normalize the amplitude among different source or receiver pairs. By applying SI by crosscoherence instead of crosscorrelation, we expect to retrieve

Table 1. Local earthquakes used in this study. (continued)

Date (month/day/year)	Time (h:min:s)	Latitude (°N)	Longitude (°E)	Depth (km)	M_b	Array ID
11/18/2012	13:29:28	−38.286	−73.690	56	4.7	TE/TN
11/19/2012	14:08:59	−33.969	−72.150	1	4.2	TE/TN
11/19/2012	16:45:50	−33.928	−72.170	11	5.1	TE/TN
11/20/2012	16:23:25	−33.921	−72.254	16	5.4	TE/TN
11/21/2012	18:16:38	−33.931	−72.100	19	5.1	TE/TN
11/21/2012	21:36:23	−33.939	−71.868	18	5.7	TE/TN
11/21/2012	22:51:23	−34.012	−72.305	35	4.2	TE/TN
11/21/2012	22:52:29	−33.916	−71.994	16	5.2	TE/TN
11/29/2012	0:09:39	−32.910	−69.106	8	5.0	TE/TN
11/29/2012	20:40:59	−36.426	−71.082	3	4.2	TE
12/02/2012	3:29:23	−35.541	−72.766	15	4.3	TE/TN
12/04/2012	9:26:14	−32.710	−71.751	38	4.6	TE/TN
12/10/2012	15:25:47	−38.932	−72.862	33	4.8	TN
12/16/2012	22:46:11	−33.803	−71.408	63	4.7	TE/TN
12/17/2012	8:38:25	−32.342	−65.287	20	4.4	TN
12/18/2012	0:45:03	−33.645	−71.187	66	3.7	TE/TN

better S/N in terms of the phase in comparison with the crosscorrelation (e.g., Prieto et al., 2009; Nakata et al., 2011). To apply SI by crosscoherence, we rewrite equation 3 as

$$2Re\{G_{z,z}^{v,t}(\mathbf{x}_A, \mathbf{x}_B, \omega)\} \propto \sum_{S=1}^{n} \frac{\{v_z^c(\mathbf{x}_A, \omega)\}^* v_z^c(\mathbf{x}_B, \omega)}{|v_z^c(\mathbf{x}_A, \omega)||v_z^c(\mathbf{x}_B, \omega)| + \varepsilon}, \tag{4}$$

where ε denotes a stabilization factor (also called a damping factor or a regularization parameter). Because the crosscoherence enhances the signal and the noise, it is important to have data that is not dominated by noise. Note that in the above equation, the retrieved Green's function is no longer modulated by the average power spectrum of the STF, as the crosscoherence eliminates it.

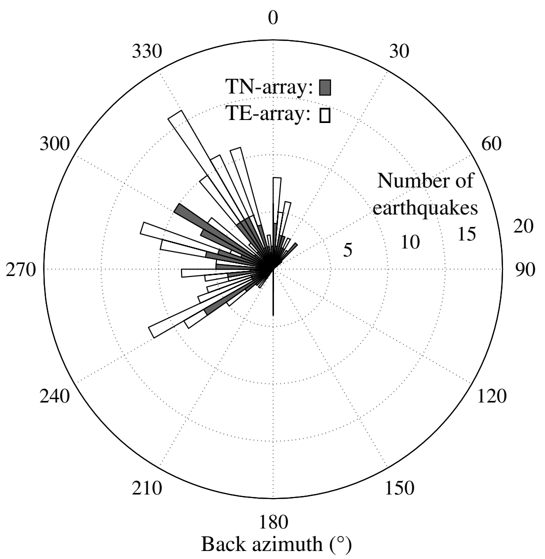

Figure 2. Distribution of the back azimuth of the local earthquakes recorded by the TN- and TE-arrays.

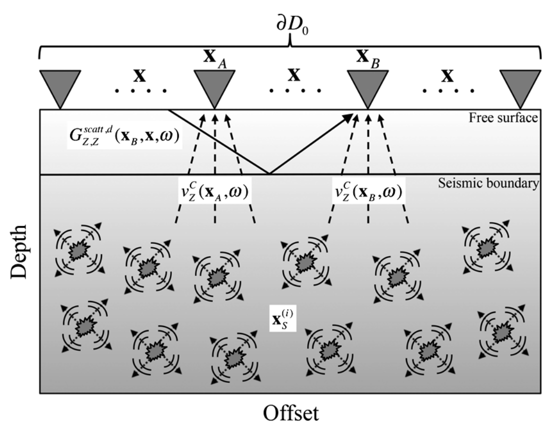

Figure 3. A schematic illustration of equation 5.

Multidimensional deconvolution

Although the aforementioned crosscorrelation and crosscoherence calculate the reflection response trace by trace, MDD is a receiver-array-based SI method that calculates the reflection response (the scattered Green's function in Wapenaar et al., 2011) simultaneously for all observed responses via matrix inversion. Although the application of MDD requires regularly spaced receivers, a point-spread function (PSF), and a regularization approach for the matrix inversion, this technique theoretically removes the influence of the (variation of the) STF of the sources, takes intrinsic attenuation into account (which is not the case for correlation nor coherence), and compensates for possibly inhomogeneous illumination of the receivers by the coda wavefield.

The PSF is a well-known gauge for imaging quality in optics, such as microscopy. In exploration seismology, the PSF is used to quantify the effect of the source and receiver distribution and of the STF on the imaging results. In analogy with this, van der Neut et al. (2010, 2011) show that the result from SI by crosscorrelation could actually be seen as the blurring (temporal and spatial convolutions) of the desired scattered Green's function with a PSF. This PSF is obtained from the crosscorrelation of recordings at the receivers at the surface as if above the receivers there were a homogeneous half-space (e.g., Wapenaar et al., 2011). Nakahara and Haney (2015) recently show that the PSF could also be used for studying earthquake sources. Application of SI by MDD is actually deconvolving the crosscorrelation result by the PSF. To obtain the required wavefield for the retrieval of the correlation result and the PSF, one can apply wavefield decomposition at the earth's surface (Nakata et al., 2014). This, though, would require a good velocity model for the near surface, which in areas, such as Malargüe, characterized by strong lateral inhomogeneity, is not readily available. Because it is not possible to obtain measurements as if the earth's surface were covered by a homogeneous half-space, following Wapenaar et al. (2011), we use an approximate relation for the application of SI by MDD:

$$\sum_{S=1}^{n} [\{v_z^c(\mathbf{x}_A, \omega)\}^* v_z^c(\mathbf{x}_B, \omega)] - 2\Gamma(\mathbf{x}_B, \mathbf{x}_A, \omega)$$
$$\propto \iint_{\partial D_0} G_{z,z}^{\mathrm{scatt},d}(\mathbf{x}_B, \mathbf{x}, \omega)\Gamma(\mathbf{x}, \mathbf{x}_A, \omega) d^2\mathbf{x}, \tag{5}$$

where Γ is the approximated PSF and $G_{z,z}^{\mathrm{scatt},d}$ is the scattered Green's function due to a dipole source. Figure 3 shows a schematic image of the terms in equation 5. The integral in equation 5 is taken along the receiver positions (earth's surface ∂D_0). A derivation of equation 5 is given in Appendix A. Just like Wapenaar et al. (2011), we look at the recorded wavefield as a part that will be recorded at the receivers in the absence of a free surface and a part due to the presence of the free surface (which is the former after being reflected at the free surface at least once). The Γ in equation 5 can be estimated by extracting time-windowed signals from the crosscorrelation at $\mathbf{x}_A$ and $\mathbf{x}_B$ (the right side of equation 3) of the wavefield that would be recorded in the absence of a free surface at the receivers. The signals that make up Γ exhibit a butterfly-shaped window approximately $t = 0$, narrowest when $\mathbf{x}_A = \mathbf{x}_B$. We assume that the contribution from the crosscorrelation at $\mathbf{x}_A$ and $\mathbf{x}_B$ of the wavefield that would be recorded due to the presence of a free surface at the receivers is sufficiently small to be neglected (van der Neut et al., 2010; Wapenaar et al., 2011). Note that the numerical test showed that the approximation can provide the correct scattered Green's function with small inversion artifacts (van der Neut et al., 2010). For notational simplicity, we define the left side of equation 5 as

$$C'(\mathbf{x}_B, \mathbf{x}_A, \omega) = \sum_{S=1}^{n} [\{v_z^c(\mathbf{x}_A, \omega)\}^* v_z^c(\mathbf{x}_B, \omega)] - 2\Gamma(\mathbf{x}_B, \mathbf{x}_A, \omega). \quad (6)$$

Substituting equation 6 in equation 5, we obtain

$$C'(\mathbf{x}_B, \mathbf{x}_A, \omega) \propto \iint_{\partial D_0} G_{z,z}^{\mathrm{scatt},d}(\mathbf{x}_B, \mathbf{x}, \omega)\Gamma(\mathbf{x}, \mathbf{x}_A, \omega) d^2\mathbf{x}. \quad (7)$$

Equation 7 can be discretized by fixing the position of $\mathbf{x}_B$ and varying the receiver position $\mathbf{x}_A$

$$\begin{pmatrix} C'(\mathbf{x}_B, \mathbf{x}_1, \omega) \\ C'(\mathbf{x}_B, \mathbf{x}_2, \omega) \\ \vdots \\ C'(\mathbf{x}_B, \mathbf{x}_m, \omega) \end{pmatrix} \propto \begin{pmatrix} \Gamma(\mathbf{x}_1, \mathbf{x}_1, \omega) & \Gamma(\mathbf{x}_2, \mathbf{x}_1, \omega) & \cdots & \Gamma(\mathbf{x}_m, \mathbf{x}_1, \omega) \\ \Gamma(\mathbf{x}_1, \mathbf{x}_2, \omega) & \Gamma(\mathbf{x}_2, \mathbf{x}_2, \omega) & \cdots & \Gamma(\mathbf{x}_m, \mathbf{x}_2, \omega) \\ \vdots & \vdots & \ddots & \vdots \\ \Gamma(\mathbf{x}_1, \mathbf{x}_m, \omega) & \Gamma(\mathbf{x}_2, \mathbf{x}_m, \omega) & \cdots & \Gamma(\mathbf{x}_m, \mathbf{x}_m, \omega) \end{pmatrix} \times \begin{pmatrix} G_{z,z}^{\mathrm{scatt},d}(\mathbf{x}_B, \mathbf{x}_1, \omega) \\ G_{z,z}^{\mathrm{scatt},d}(\mathbf{x}_B, \mathbf{x}_2, \omega) \\ \vdots \\ G_{z,z}^{\mathrm{scatt},d}(\mathbf{x}_B, \mathbf{x}_m, \omega) \end{pmatrix}, \quad (8)$$

where we assume that we have m receivers in total. We can simplify equation 8 using matrix-vector notation

$$\mathbf{c}' \propto \mathbf{\Gamma}\mathbf{g}, \quad (9)$$

where $\mathbf{\Gamma}$ is a $m \times m$ matrix and $\mathbf{c}'$ and $\mathbf{g}$ are $m \times 1$ column vectors showing receiver gathers. Constructing multiple column vectors using equation 8 for variable $\mathbf{x}_B$ and arranging them as columns of a matrix, we obtain

$$\mathbf{C}' \propto \mathbf{\Gamma}\mathbf{G}, \quad (10)$$

where $\mathbf{C}'$ and $\mathbf{G}$ are $m \times m$ monochromatic matrices containing $C'(\mathbf{x}_m, \mathbf{x}_m, \omega)$ and $G_{z,z}^{\mathrm{scatt},d}(\mathbf{x}_m, \mathbf{x}_m, \omega)$, respectively. Estimating the dipole scattered Green's function in equation 10 requires matrix inversion

$$\mathbf{G}' \propto [\mathbf{\Gamma}]^{-g}\mathbf{C}', \quad (11)$$

where $[\mathbf{\Gamma}]^{-g}$ is a generalized inverse of $\mathbf{\Gamma}$ and $\mathbf{G}'$ is an estimate of $\mathbf{G}$.

Note that our receiver configuration might not be optimal for MDD studies. The number of receivers we have is relatively small — 19 and 13 for the TN- and TE-arrays, respectively. Fewer receivers lead to more severely ill-posed solutions in the inversion process. Two approaches to stabilize the MDD in equation 11 have been used: damped least squares (Menke, 1989) and singular-value decomposition (SVD) (Klema and Laub, 1980).

MDD by damped least squares

The damped least-square solution is a commonly used approach for MDD studies (e.g., Wapenaar et al., 2008; van der Neut et al., 2011; Boullenger et al., 2015). This scheme can be directly adapted to the generalized inverse matrix in equation 11, resulting in

$$\mathbf{G}' \approx [\mathbf{\Gamma}^\dagger\mathbf{\Gamma} + \varepsilon\mathbf{I}]^{-1}\mathbf{\Gamma}^\dagger\mathbf{C}', \quad (12)$$

where ε and $\mathbf{I}$ indicate a stabilization factor and the identity matrix, respectively. The symbol $\dagger$ denotes the complex conjugate transpose matrix. In practice, $\mathbf{\Gamma}$ is estimated in the time domain and then transformed to the frequency domain by the Fourier transform. A disadvantage of this scheme is that choosing an appropriate stabilization factor tends to be inevitably subjective because it is difficult to evaluate the data redundancy in a quantitative way.

MDD by truncated singular-value decomposition

There are only a few examples of MDD based on the truncated SVD scheme (e.g., Minato et al., 2011, 2013). The concept of the truncated SVD scheme is fundamentally close to the principal component analysis (Pearson, 1901) in machine learning, which is also called a subspace method or Karhunen-Loève expansion, and the latent semantic analysis (Borko and Bernick, 1963) in natural language processing. For example, the truncated SVD scheme and principal component analysis find the data directions (axes) from the eigenvectors of the covariance matrix using the SVD algorithm via the Lagrange multiplier. Here, we briefly introduce the truncated SVD scheme.

Let us define the SVD of $\mathbf{\Gamma}$ in equation 10 as

$$\mathbf{\Gamma} = \mathbf{U}\begin{pmatrix} \mathbf{\Delta}_r & \mathbf{0} \\ \mathbf{0} & \mathbf{0} \end{pmatrix}\mathbf{V}^{\dagger}, \qquad (13)$$

where $\mathbf{U}$ is a left-singular matrix (orthonormal-basis matrix), $\mathbf{V}$ is a right-singular matrix (orthonormal-basis matrix), $\mathbf{V}^{\dagger}$ is the adjugate (adjoint) matrix that is the complex conjugate transpose matrix of $\mathbf{V}$, and $\mathbf{\Delta}_r$ is an $r \times r$ diagonal matrix, whose elements are the singular values of the monochromatic matrix $\mathbf{\Gamma}$, obtained by truncation. We define the dimension r as the number of significant singular values by specifying a threshold value. Then, we adapt the Moore-Penrose pseudoinverse (Golub and van Loan, 1983) for equation 13

$$[\mathbf{\Gamma}]^{-g} = \mathbf{V}\begin{pmatrix} \mathbf{\Delta}_r^{-1} & \mathbf{0} \\ \mathbf{0} & \mathbf{0} \end{pmatrix}\mathbf{U}^{\dagger}, \qquad (14)$$

where $\mathbf{U}^{\dagger}$ is the adjugate (adjoint) matrix of $\mathbf{U}$. In the following section, we show the MDD results of the damped least-squares scheme and the truncated SVD scheme.

Data processing

Preprocessing

Our first step in the preprocessing is to remove the instrument response from the recorded data. After that, we compute power spectral densities (PSD) of the local earthquakes to determine a frequency band that exhibits its adequate S/N. Examples of PSD of the local earthquake for the TE-array are shown in Figure 4. Analyzing the PSDs, we choose the frequency band 1–5 Hz for further seismic processing. We set the high end of the band at 5 Hz due to the presence of irregular noise approximately 8 Hz (see Figure 4), which is masking the signals from weaker earthquakes. The nature of this noise is not clear. The stations are away from continuous anthropogenic sources, so this could be excluded as main contributor. Because this noise is almost continuously seen over the records in MalARRgue, it might be connected to the wave action in the nearby lake Llancanelo (Figure 1), but possibly also with deeper activity below the volcanic cones in the vicinity of the array. The noise, which is also continuously seen at approximately 0.3 Hz, likewise to be due

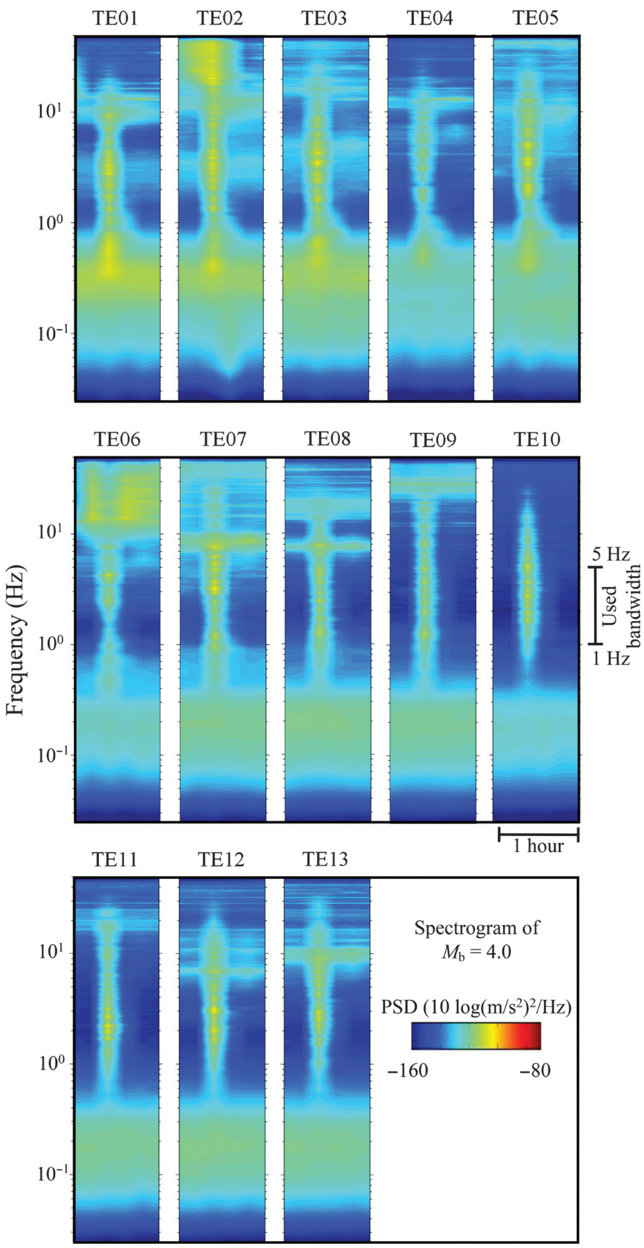

Figure 4. The PSDs for a local earthquake with M_b 4.0 and they are computed for the TE-array.

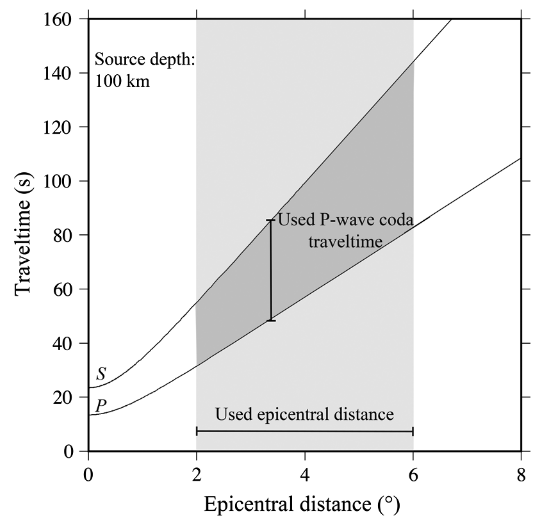

Figure 5. Used window length of the P-wave coda as a function of epicentral distance. The traveltime curves are drawn using the regional velocity model from Farías et al. (2010) for depths down to 110 km and the ak135 model (Kennett et al., 1995) for greater depths. Light gray rectangular indicates the used epicentral distance, whereas the dark gray area indicates the window lengths to be extracted for an earthquake characterized by a source depth of 100 km.

to the double-frequency microseisms. In principle, one can use a higher frequency (if available) for LEPC SI to obtain images of shallower structures, e.g., at the basin scale. For speeding up the computations, after the band-pass filtering, we downsample the data to 0.05 s (Nyquist frequency of 10 Hz) from the original sampling of 0.01 s (Nyquist frequency of 50 Hz).

The useful window length of the coda of the P-wave phase is explained in Figure 5 as a function of the epicentral distance. To calculate the times in Figure 5, we use the regional velocity model of Farías et al. (2010) down to 110 km and ak135 (Kennett et al., 1995) deeper than that. To only extract the P-wave coda without the direct wave that usually brings strong directivity in the SI results, we refer to the scaling relation between the moment magnitude M_W and the source duration of the earthquakes (Kanamori and Brodsky, 2004) assuming that M_W is proportional to M_b for our magnitude range (Atkinson and Boore, 1987). Thus, our coda-wave extraction window starts at the time obtained from the summation of the time of the expected P-phase arrival and the expected time length of the STF.

For local earthquakes ($2° \leq$ epicentral distances $\leq 6°$), surface waves are expected to arrive almost simultaneously with the S-wave phase onset or later (Kennett et al., 1995). To make sure that the coda does not contain surface waves related to the earthquake, our coda-wave extraction window terminates a few seconds before the observed S-wave phase onset.

With the above window-length selection criteria, the coda duration is shorter for some earthquakes, but still we have sufficient coda duration (e.g., 15–70 s) for the subsurface imaging. An example of the coda extraction is shown in Figure 6. For subsequent seismic processing, we use only the P-wave coda (the blue window) extracted from the vertical component. It is difficult to estimate how many converted S-wave phases are present within the P-wave coda, but they most probably are present. Especially, SV-waves are expected to be present on the vertical component we use. In this study, we assume that the SV-waves are not dominantly recorded for deeper earthquakes (e.g., 50–100 km) due to their small slowness. For shallower earthquakes (e.g., 0–50 km), the SV-waves can be recorded with spatial aliasing due to the larger ray parameter compared with the ray parameter for P-waves. However, the crosscorrelation and summation process should suppress such aliasing effects, emphasizing the reflection responses of the structures. Note that the transverse component in Figure 6 is displayed only for the purpose of data comparison with the vertical component.

After extracting the P-wave coda from each selected local earthquake, we interpolate missing traces at certain stations (e.g., due to technical problems in the acquisition) using their two closest neighboring station records using linear interpolation. For example, if TE10 has a missing trace, we interpolate it only when TE09 and TE11 have nonmissing traces for that time. In Figure 7, we show the number of interpolated traces (what we also call events).

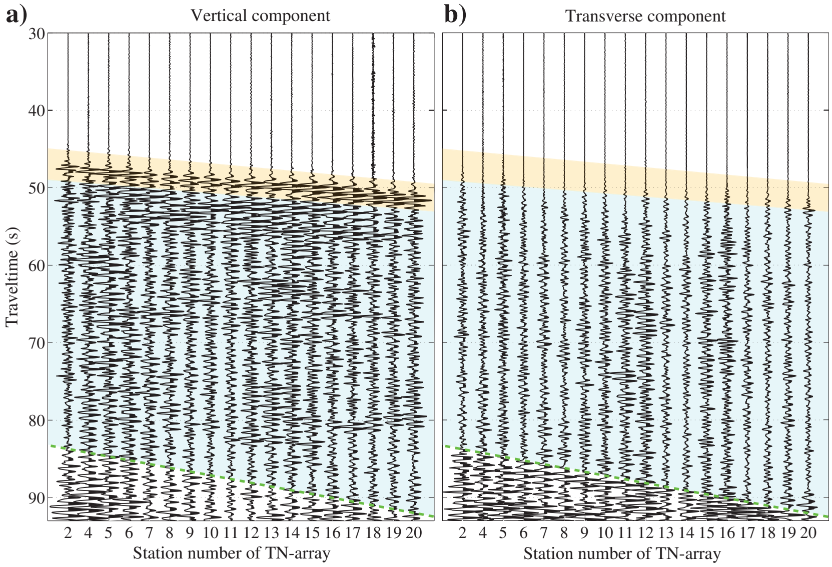

Figure 6. An example recording of a local earthquake on (a) the vertical and (b) transverse components of the stations from the TN-array. The areas highlighted in orange indicate the direct P-wave arrival from the local earthquake, whereas the green lines indicate the S-wave onset. The area highlighted in light blue indicates the P-wave coda to be extracted.

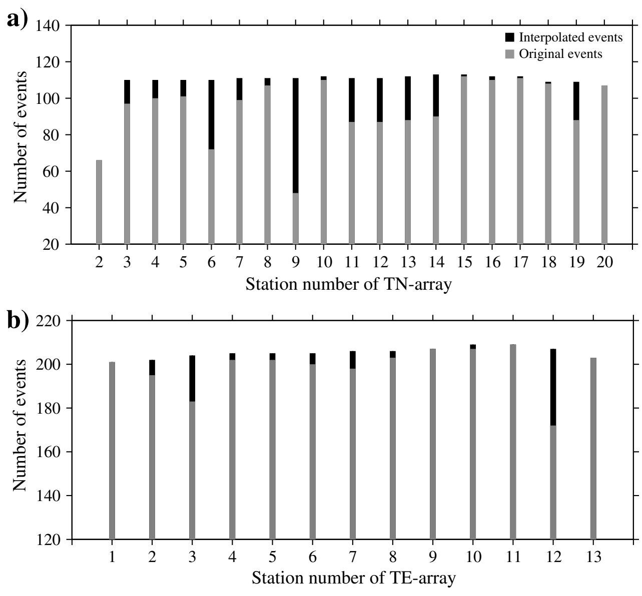

Figure 7. Number of original and interpolated events for each of the (a) TN- and (b) TE-array stations.

LEPC SI applications

Crosscorrelation and crosscoherence processing

We apply crosscorrelation to the preprocessed data of the T-array from MalARRgue after applying amplitude normalization per coda-wave window per station. The normalization is used to bring per station the correlation results from each local earthquake to a comparable amplitude and thus to let each correlation have the same weight in the summation over the earthquakes. We test usage of energy normalization, normalization by the maximum amplitude, and normalization by the maximum amplitude followed by spectral whitening. In Figure 8b–8d, we show the three respective results obtained from autocorrelation, which represent retrieved zero-offset traces. In Figure 8a, we show the retrieved zero-offset trace obtained without any normalization. As can be seen from Figure 8a–8c, there is no significant difference between the results with and without normalizations, implying that for the earthquakes we choose, the recordings from the different earthquakes have comparable amplitudes in the 1–5 Hz frequency band. Nevertheless, we can notice small differences among the results, so it is better to use normalization before correlation given its numerical robustness. In Figure 8e, we show the retrieved zero-offset trace obtained from autocoherence. In Figure 8d, we show for completeness of comparison another correlation result obtained after energy normalization and spectral whitening. The whitening was performed using a running window of 0.025 Hz width. Note that energy normalization followed by spectral whitening makes the result retrieved by correlation (Figure 8d) close to the one retrieved by coherence (Figure 8e). This is because normalization and spectral whitening mathematically approximate coherence. In this study, we use crosscorrelation and crosscoherence. For retrieval using crosscorrelation, we choose to use preprocessing by energy normalization without spectral whitening (as in Figure 8b), so that we could see clear differences between the results from crosscorrelation and those from crosscoherence.

Figure 9a and 9d shows retrieved common-source gathers (at positive and negative times) obtained using crosscorrelation for a virtual source at TN11 (the middle station in the TN-array) and TE07 (the middle station in the TE-array), respectively. It can be seen that the common-source gathers exhibit asymmetrically retrieved events with respect to two-way traveltime 0 s, indicating that the coda we use is not illuminating the stations equally from all directions. Even though Mayeda et al. (2007), Baltay et al. (2010), and Abercrombie (2012) assume apparent weak to no directivity of the coda, i.e., isotropic energy flux, due to the expected averaging out of radiation pattern of the earthquake, Paul et al. (2005) and Emoto et al. (2015) find that the energy flux of the coda is not isotropic. In the case that the coda has no directivity, the causal and acausal parts of the common-source gathers obtained from crosscorrelation would result in a purely symmetric gather. When the coda has directivity, the common-source gather would exhibit asymmetry as shown in Figure 9d.

A possible explanation of the directivity in the coda, which is most likely the case with our data as well, is that it is associated with the direct-wave passages (e.g., Emoto et al., 2015). Emoto et al. (2015) discuss that the coda consists of forward scattered waves (early coda), which have directivity, and multiply scattered waves (later coda), which have no directivity.

For the results retrieved from SI by crosscorrelation and crosscoherence, we correct for the asymmetric results (Figure 9a and 9d) by combining part of the positive and parts of the negative times as follows. To obtain a final retrieved common-source gather, we use the acausal part of the retrieved result for traces to the west of the virtual-source position, reverse this part in time, and concatenate it to the causal part of the retrieved result for traces to the east of the virtual-source position (Figure 9b and 9e). This processing is strictly valid for a horizontally layered medium. In our case because we rely on secondary scattering, we can still use this processing provided that the scattering results in the illumination of the array mainly from the west of the

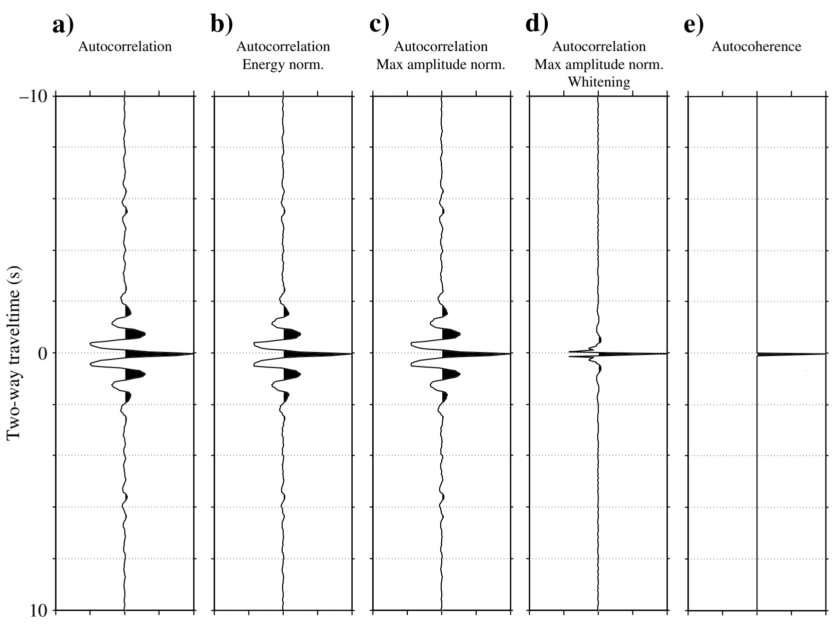

Figure 8. Retrieved zero-offset trace at station TE07 of the TE-array obtained using (a) autocorrelation without amplitude normalization, (b) energy normalization before autocorrelation, (c) maximum-amplitude normalization before autocorrelation, (d) maximum-amplitude normalization followed by spectral whitening before autocorrelation, and (e) autocoherence.

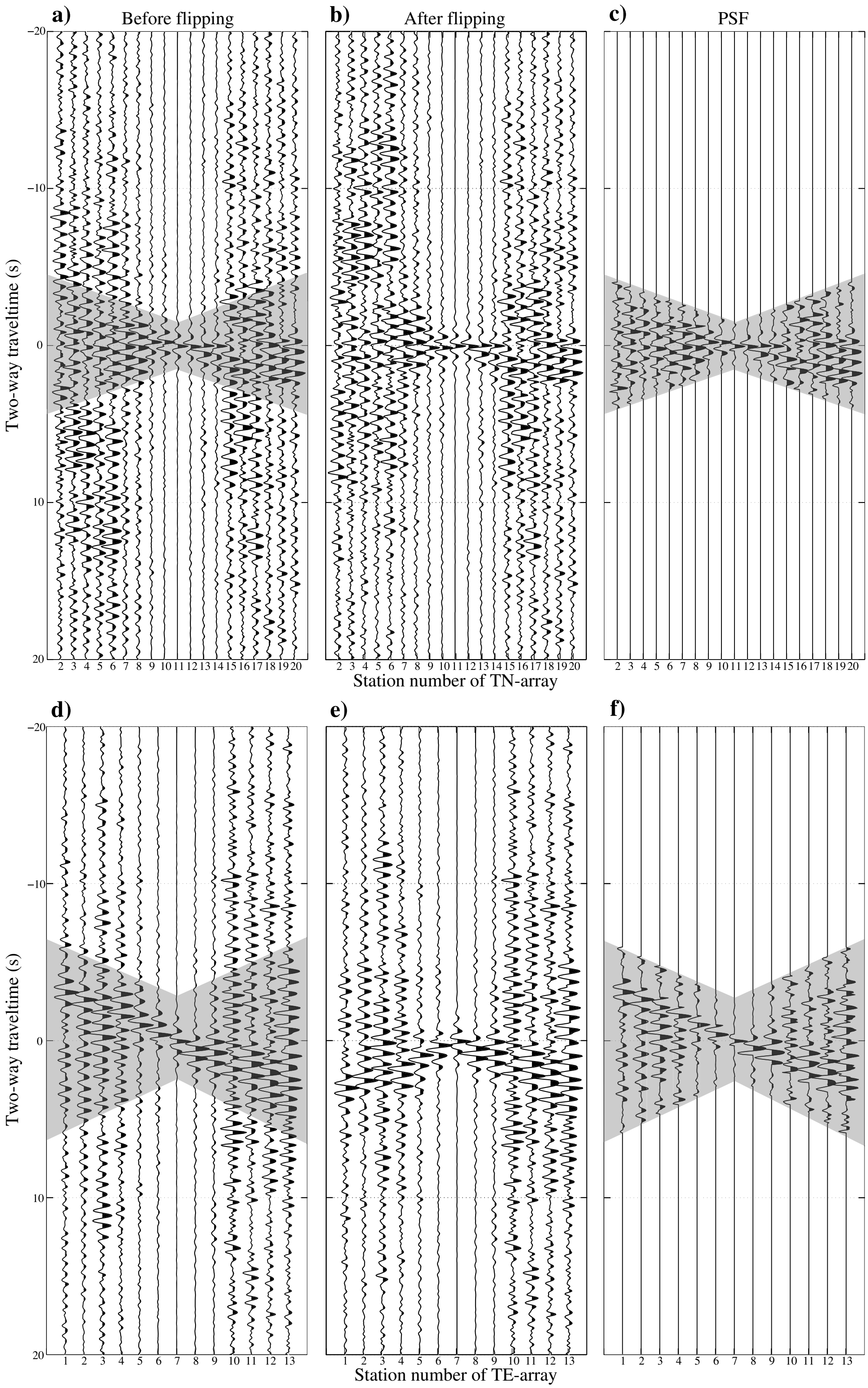

Figure 9. Retrieved common-source gather for a virtual source at (a) station TN11 of the TN-array before flipping, (b) after flipping the negative times, (d) station TE07 of the TE-array before flipping, (e) after flipping the negative times. The PSFs of panels (c and f) are extracted from the gray shaded areas in panels (a and d), respectively. The results are retrieved using correlation and after summation over the used local earthquakes.

array and that the structures below the array are not complex.

For the next processing step, we apply a deterministic spiking deconvolution to remove the STF of the retrieved virtual source from each of the retrieved common-source gathers. The deterministic spiking deconvolution is a technique that compress the STF (e.g., known from observation) using the least-squares method. The STF are estimated from the retrieved zero-offset traces at each virtual-source position by extracting a time-window approximately time 0 s (Figure 10). Following the conventional seismic processing, we mute the first breaks and all the events above them from the common-source gathers for the TN- and TE-arrays as shown in Figure 11. Our estimates of the first breaks are approximately 3400 m/s (a constant velocity) for both arrays. After that, we resort the traces into CMP gathers and apply NMO velocity analysis to the data using semblances. In Figure 12, two examples of velocity semblance are shown with the regional velocity model by Farías et al. (2010) indicated by the dashed magenta lines. There is good correspondence between the regional model and peaks in the middle part of the semblance. For example, the bright spots

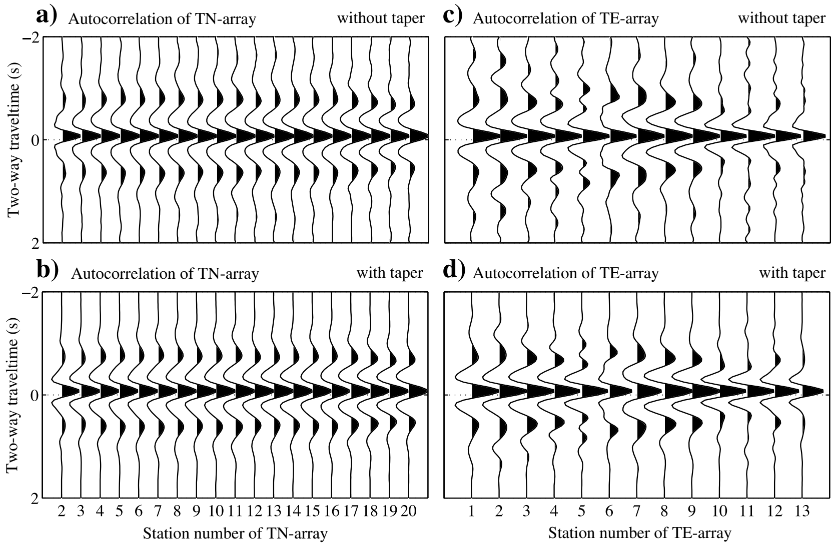

Figure 10. Retrieved zero-offset traces using all events from (a) the TN- and (c) the TE-arrays. (b and d) Estimated STF from the zero-offset traces in panels (a and c), respectively, after application of time windowing.

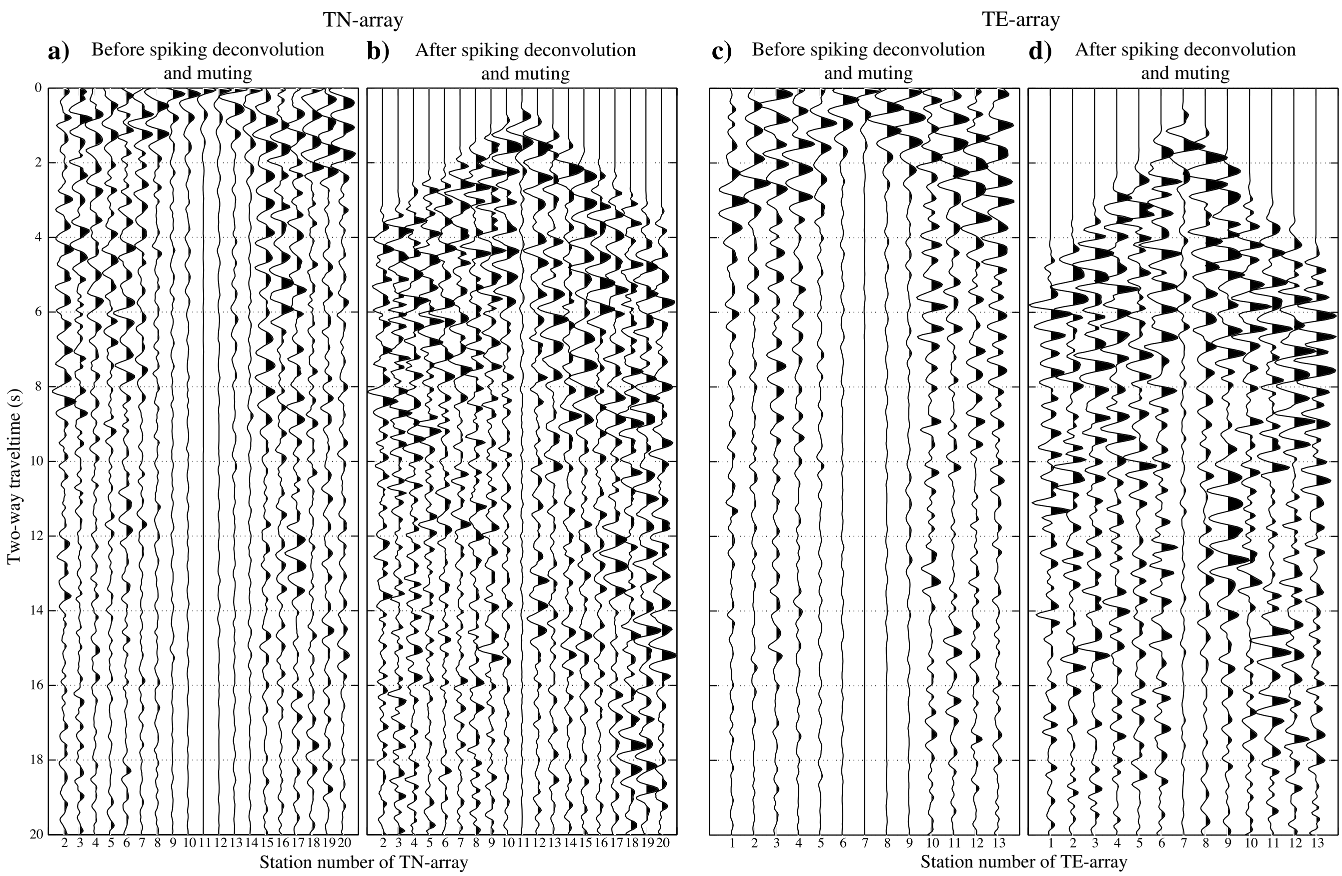

Figure 11. A comparison of common-source gather: for station TN11 of the TN-array (a) before spiking deconvolution and muting the first breaks and (b) after spiking deconvolution and muting the first breaks and above; for station TE07 of the TE-array (c) before spiking deconvolution and muting the first breaks and (d) after spiking deconvolution and muting the first breaks and above.

in the semblance at approximately 10–11 s (Figure 12a) correspond to the range of the possible Moho velocity in Farías et al. (2010). In this study, though, for NMO correction and migration, we use the regional velocity model from Farías et al. (2010) because this simplifies the interpretation during the comparison of the current result with our previous result from application of global-phase SI (Nishitsuji et al., 2016). Global-phase SI is an autocorrelation SI that uses global phases (e.g., PKiKP).

After obtaining stacked sections along both arrays, we apply predictive deconvolution to suppress possible multiples from the top basement using the estimated depth of the top of the basement beneath MalARRgue (Nishitsuji et al., 2014). Finally, we apply Kirchhoff post-stack time migration (KTM) (Yilmaz, 1987) to move dipping structures to their true location in the model. As a final processing step, we apply lateral regularization in the horizontal direction to obtain better imaging in terms of structural interpretation. For the lateral regularization, we use smoothed discretized splines determined by the generalized crossvalidation (Garcia, 2010). The stacked sections before and after the mentioned processing (predictive deconvolution, KTM, and lateral regularization) for the TN- and TE-arrays are shown in Figures 13a and 13b and 14a and 14b, respectively.

The seismic processing of the results retrieved from SI by crosscoherence is the same as for the results retrieved by crosscorrelation, except for the step of applying spiking deconvolution of the STF, which is not needed. The processed stacked section obtained from SI by crosscoherence is displayed in Figures 13c and 14c. For Figures 13c and 14c, we select the results obtained using a stabilization factor of 1% of the maximum in the amplitude spectrum. In our case, we did not see significant differences when using stabilization factors between 1% and 5%.

MDD processing

The data processing for application of SI by MDD differs only in a few steps from the other two LEPC (crosscorrelation and crosscoherence) and interferometric applications. Due to the fact that MDD intrinsically deconvolves for the STF of the earthquake sources and compensates for directivity in the illumination, neither spiking deconvolution for the STF of the retrieved virtual source nor selective usage of parts of the causal and acausal times are needed. Instead, it is necessary to obtain the estimated PSF for solving the inverse problem of the approximated MDD in equation 11. In Figure 9c and 9f, we show two examples of PSFs extracted (cut away with

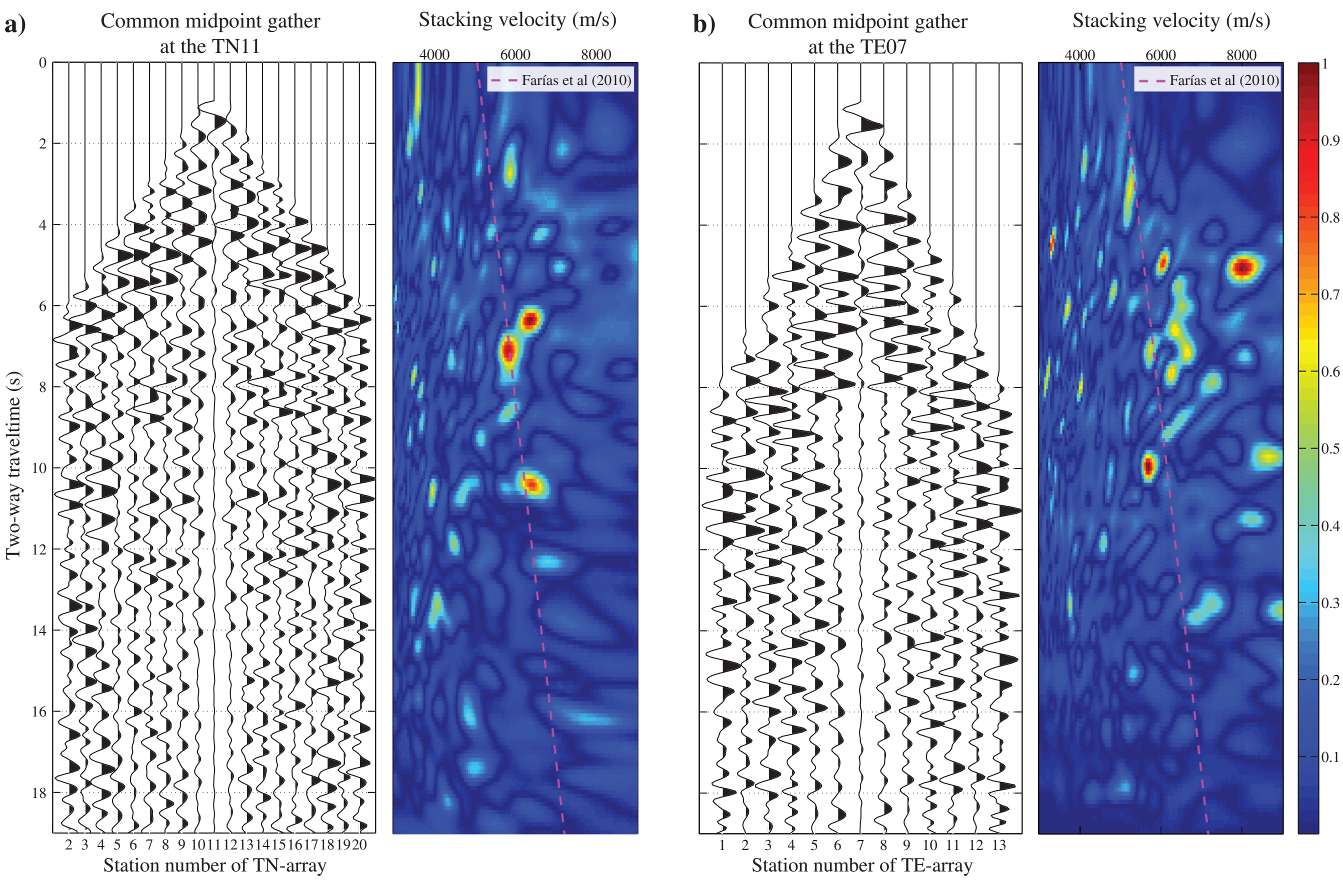

Figure 12. Examples of velocity semblance of CMP gather for (a) station TN11 of the TN-array and (b) station TE07 of the TE-array with the regional velocity model of Farías et al. (2010) denoted by the dashed magenta lines.

tapered edges) from the retrieved crosscorrelation results in Figure 9a and 9d, respectively. We extracted the PSF with a butterfly-shaped window approximately $t = 0$ and narrowest for $\mathbf{x}_A = \mathbf{x}_B$. It aims to include events obtained from the crosscorrelation between waves that are recorded at the surface as direct waves from secondary sources in the subsurface (the scatterers and reflectors). Note that the approximated PSFs are shown after amplitude normalization among the stations for the purpose of displaying only; we do not use amplitude normalization for the actual MDD processing. The time window for the PSF is based on the velocity used for the first-break muting in Figure 12.

We apply SI by MDD to the LEPC data using the truncated SVD approach to stabilize the inversion. We process the two lines separately — we retrieve virtual-source response along the TN-array using the events recorded by and interpolated along the TN-array; we retrieve virtual-source response along the TE-array using the events recorded by and interpolated along the TE-array. As can be seen from Figure 7, the number of earthquakes for each station per subarray is different. For example, for the TE-array, the number of interpolated events per station is between 200 and 210. This means that several PSFs for the TE-array contain zeros for the matrix inversion. However, we expect that the illumination compensation for the TE-array from the used 210 events will be affected only to a small degree by the zeros in the PSFs due to the random distribution of the zeros. The same can be said for the TN-array as well, but in its case, the number of interpolated events per station is approximately 115 (except for TN02). After the SVD, we truncate singular values with amplitudes with a threshold value of 10% of the maximum singular value. The singular values under the threshold are considered negligible to retrieve reflection-data estimates. Figure B-1 is available in Appendix B that shows the singular values we truncate. The discarded singular values would largely contribute to the ill-posedness of equation 11. In Figure 15a and 15b, we show the obtained MDD results in the f-x domain for virtual shots at TN11 and TE07, respectively. We also test the application of SI by MDD using the damped least-squares stabilization with a constant stabilization factor for all frequencies, but the results are not as well stabilized as the ones using the truncated SVD scheme (Figure 15).

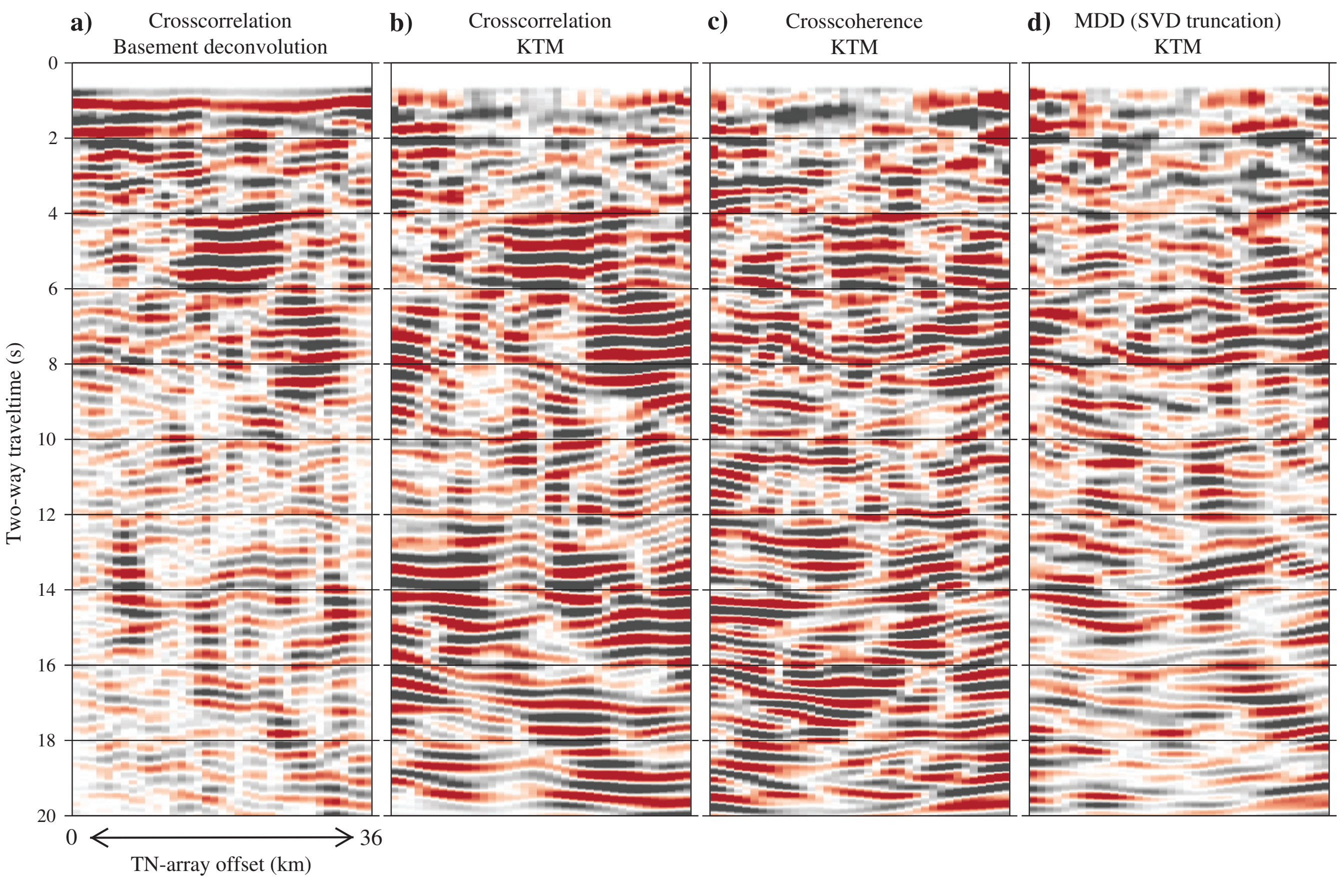

Figure 13. A comparison of LEPC SI results for the TN-array using different SI theories: (a) crosscorrelation after basement deconvolution without KTM; (b) the same as panel (a), but with KTM; (c) same as panel (b), but for crosscoherence; (d) the same as panel (b), but for MDD using the truncated SVD scheme.

Results and interpretation

In Figures 16 and 17, we show the LEPC SI results for the TN- and TE-arrays, respectively, obtained by MDD using the truncated SVD; we compare these results with the results obtained by global-phase SI by Nishitsuji et al. (2016), who use frequency band 0.3–1 Hz. We design the processing parameters for the basement predictive deconvolution based on the estimated two-way traveltime of the basement multiples (Nishitsuji et al., 2014). For comparison purposes, we use the same processing parameters of KTM for the LEPC SI and the global-phase SI results. The reflection imaging exhibits more details than the results from the global-phase SI. The bifurcated Moho and the magma chamber indicated in Figures 16 and 17 are after Gilbert et al. (2006). The gray shades in Figures 16 and 17 indicate the offset where the CMP fold numbers are less than or equal to 5; we do not interpret the results inside the gray shaded areas because we deem this fold insufficient for imaging. The dashed yellow lines are our structural interpretation where the amplitude and phase discontinuities are seen based on the global-phase SI results. We superimpose those interpreted features over the LEPC SI results because it is difficult to tell which features are the artifacts or not in a decisive way. Although one might like to interpret more structures on the LEPC SI results, we only focus on the major features interpreted by the global-phase SI results. Because we would like to keep the correspondence, no horizon interpretations are given for structures shallower than approximately 7 s two-way traveltime, where the global-phase SI results become unclear (Figures 16b and 17b). The global-phase SI results (Figures 16b and 17b) show the limitation in interpreting shallow structures because the subtraction of the average STF for 10 s unavoidably removes some shallow structures. Note that because LEPC SI has retrieved reflections that resulted in imaging structures below the array, we can conclude that there has been sufficient local scattering below the array. This is also expected from the presence of a line of volcanic cones at the surface crossing the TE-array. Local secondary scattering from structures below the array would result in arrivals characterized by small emergence angles at the array; such arrivals will be turned by SI into reflections. Because the local earthquakes we use are distanced from the TN- and TE-arrays and the coda window length is limited, if there were little or no local scattering below the array, LEPC SI would not have retrieved reflections.

Because all of the LEPC SI results (crosscorrelation, crosscoherence, and MDD) appear in general to be similar (see Figures 13b–13d and 14b–14d), one might

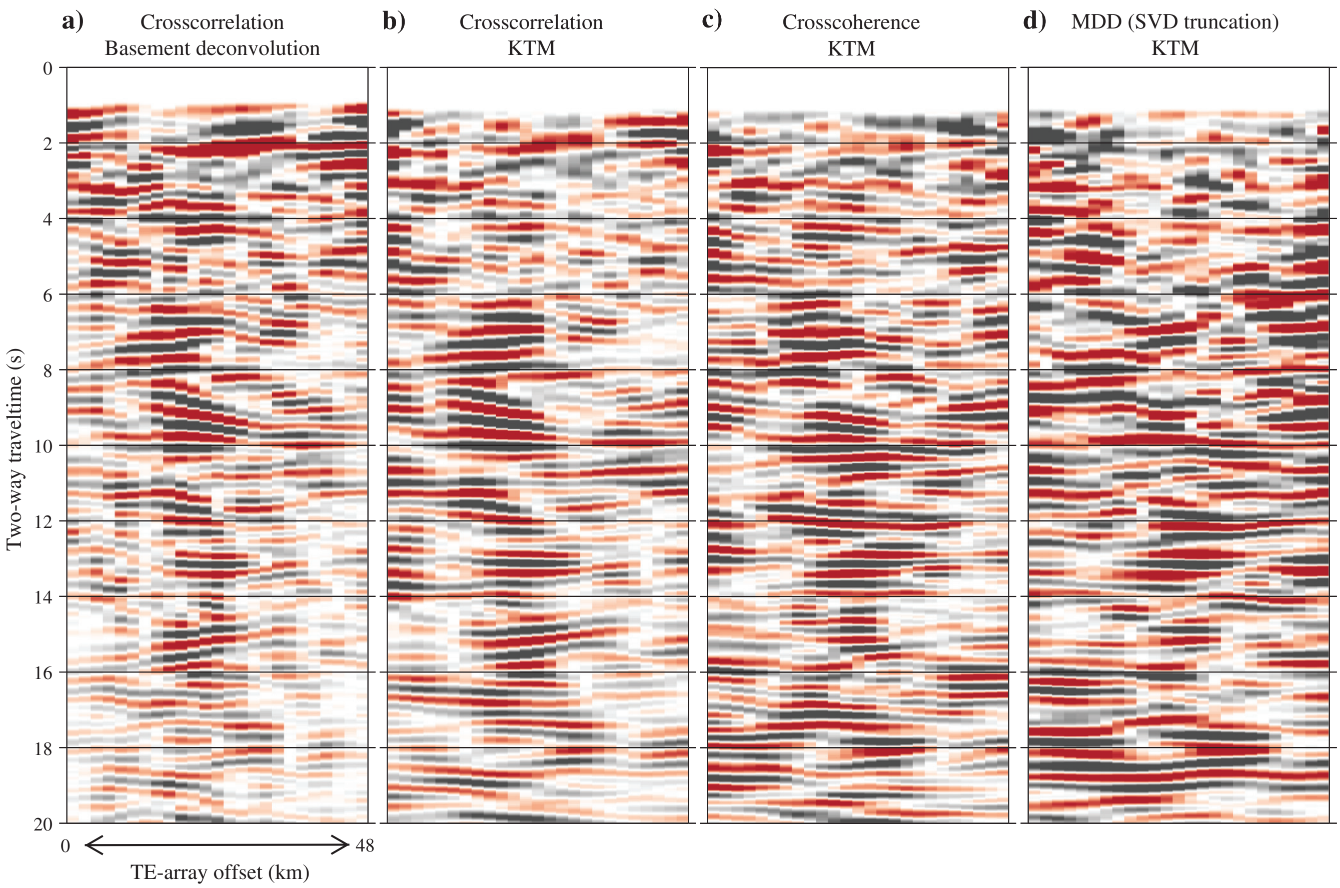

Figure 14. Same as Figure 13, but for the TE-array.

prefer to use for the interpretation of the other LEPC SI results instead of the MDD results. However, if we have a limited number of local earthquakes whose back-azimuth coverage is insufficient with respect to the receiver array, MDD should in theory work better than the other two methods (Nakata et al., 2014). This is,

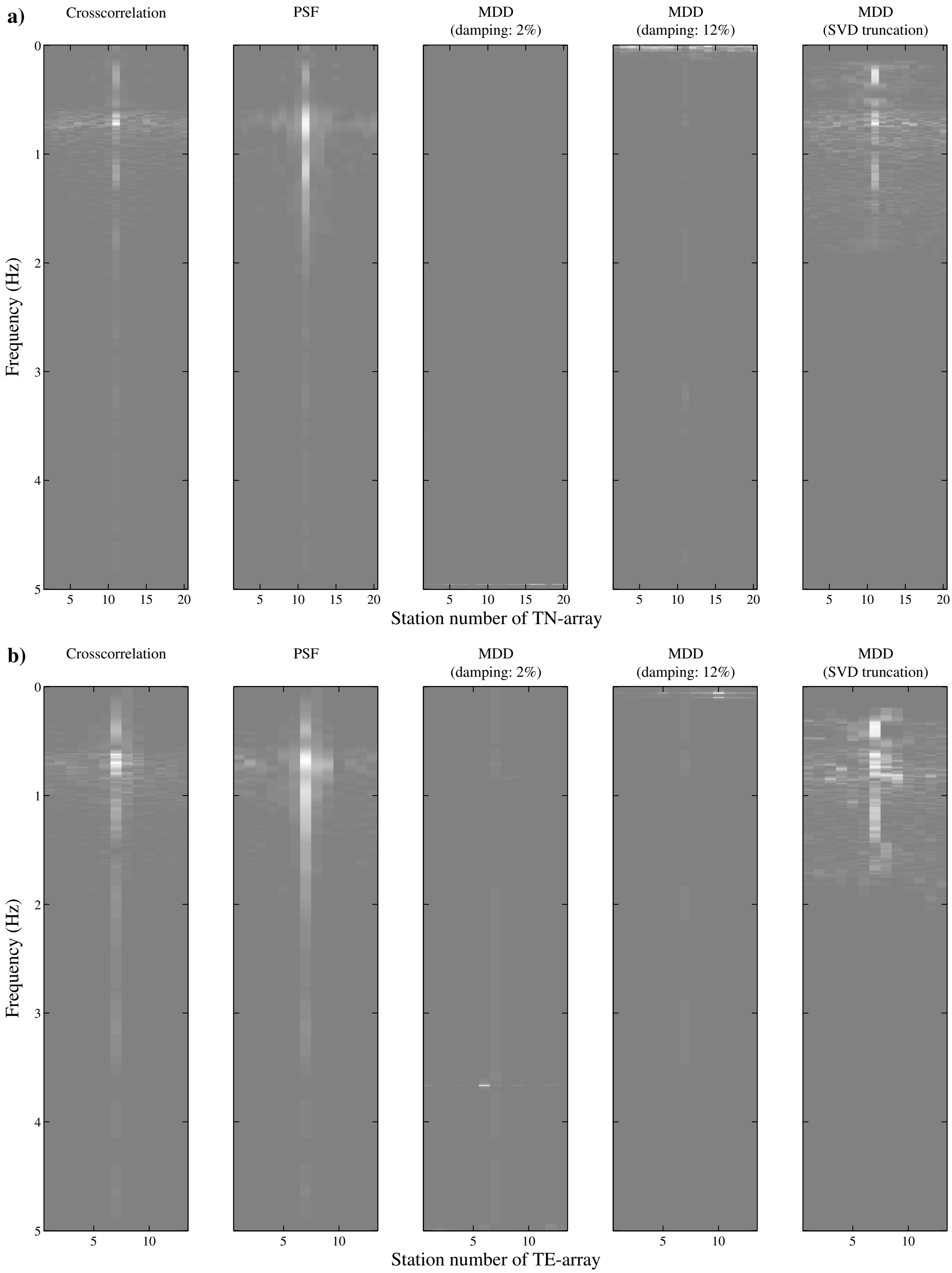

Figure 15. Obtained MDD results using damped least squares and the truncated SVD scheme in the f-x domain for virtual shots at (a) station TN11; (b) station TE07 in comparison with the crosscorrelation (Figure 9a and 9d) and the PSF (Figure 9c and 9f).

because for crosscorrelation and crosscoherence to work, a large number of local earthquakes with sufficiently wide back-azimuth coverage is essential for the effective suppression of the crosstalk (e.g., Snieder, 2004; Snieder et al., 2006). On the other hand, assuming a sufficiently good coverage of the local earthquakes is available, but the receiver-array is patchy or irregular, crosscorrelation and crosscoherence would work, whereas MDD would be ill-posed because it requires regularly spaced receivers. As shown in Figures 1 and 2, we have good coverage of the local earthquakes recorded at the exploration-type array. This could be the reason why the LEPC SI results in Figures 13b–13d and 14b–14d show similar results at our scale of interest. Nevertheless, we decide to select the LEPC SI results based on the MDD by truncated SVD scheme in Figures 16 and 17 rather than the others because we find that a few structural features showing more continuity in space. For instance, a horizontal coherent feature approximately 8 s in Figure 16 and up-dipping (from west to east direction) structures between 13 and 15 s in Figure 17 are clearer than the images from the other two methods in Figures 13 and 14. More importantly, the PSFs in Figure 15 are smeared in space and time, which means that the crosscorrelation results in Figures 13 and 14 are biased due to the spatial-temporal blurring effect of the PSF. This is also the reason we select the MDD results in Figures 16 and 17.

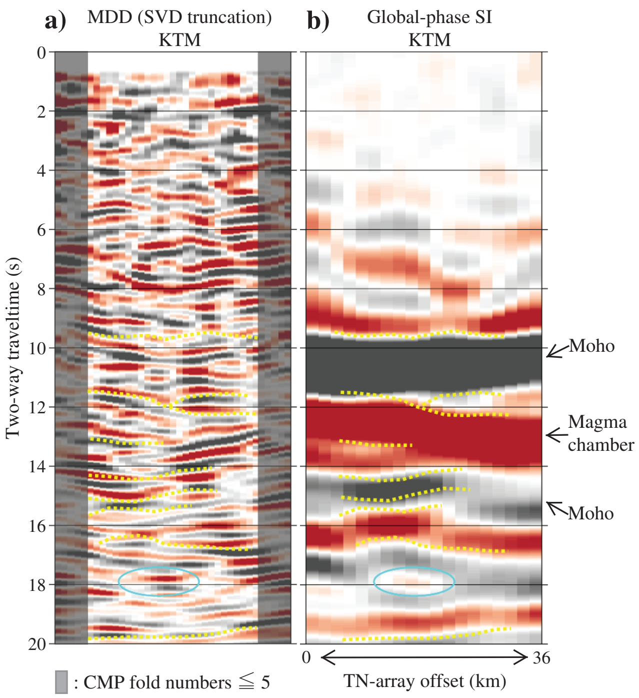

Figure 16. Summarized interpretation on the crustal-scale reflection images beneath the TN-array obtained from: (a) LEPC SI (1-5 Hz) with the truncated MDD scheme; (b) global-phase SI (0.3–1 Hz) modified from Nishitsuji et al. (2016). The interpretation of the Moho and the magma chamber is after Gilbert et al. (2006) and Nishitsuji et al. (2016). The dashed yellow lines indicate our structural interpretation that can be traced for the MDD and the global-phase SI results. The gray shades are the offset at which the CMP folds are less than or equal to 5. The cyan ellipses indicate the amplitude pockets that can be commonly interpretable between the MDD and the global-phase SI results.

Interpreting results from the magnetotelluric method, Burd et al. (2014) (the dashed blue line in Figure 1) recently suggest the presence of a possible shallow asthenospheric plume (e.g., 0–100 km in depth) nearby the Peteroa volcano. The authors interpret this shallow plume as possibly connected to the main upwelling plume, whose origin would be around the mantle transition zone (410–660 km in depth). Gilbert et al. (2006) show the receiver-function imaging at approximately 50 km south of MalARRgue, interpreting a possible bifurcation of the Moho with magma chamber in between (Figure 5 in Gilbert et al., 2006). The study by Nishitsuji et al. (2016) using the global-phase SI confirms such Moho bifurcation beneath the array of the MalARRgue. Summing up the above interpretations, one could expect a dynamic tectonic regime rather than a static one in this Andean region.

As we described earlier, the reflection imaging of the LEPC SI results exhibits more details than the results from the global-phase SI. As shown by Abe et al. (2007) and Nishitsuji et al. (2016), the vertical imaging resolution in results retrieved by SI would be at least as high as, but potentially higher than, the ones obtained by the receiver-function method. The difference of the resolution in Figures 16 and 17 is largely due to the difference in the used frequency band. Nishitsuji et al.

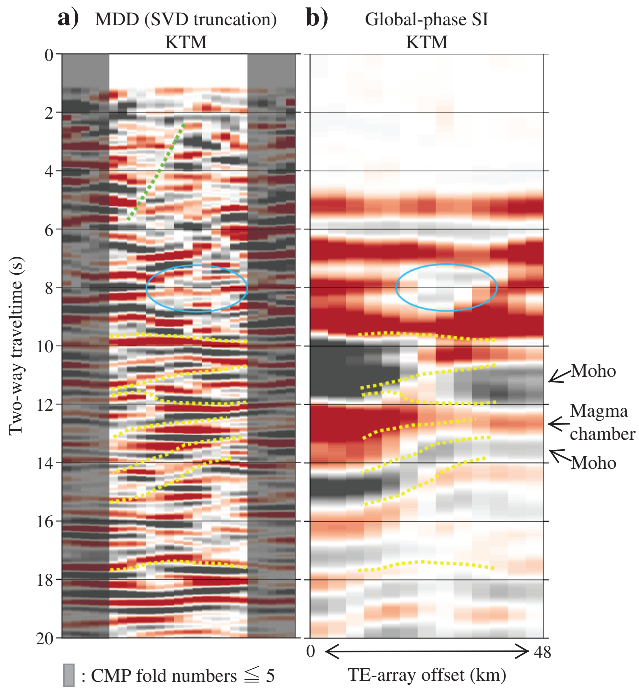

Figure 17. Same as Figure 16, but for the TE-array. The blue ellipses indicate the dimming imaging parts that can be commonly interpretable between the MDD and the global-phase SI results. The dashed green line indicates our fault interpretation, where the major deep thrust fault can be traced.

(2016) use global-phase earthquakes with frequency band 0.3–1 Hz, whereas here, we use 1–5 Hz for the LEPC SI results. In addition to the correspondence (or similarity) of the structural features (the dashed yellow lines in Figures 16 and 17) between these two different methods, there is another striking feature — a possible major fault in Figure 17a, indicated by the dashed green line, where horizon displacements can be seen. According to the active-seismic reflection profile (the solid green line in Figure 1) and nearby exploration well (LPis x-1) given in Kraemer et al. (2011), deep basement thrust faults, which are reverse faults (see Figure 8a in Kraemer et al., 2011), are expected to exist in this region as a typical feature of foredeep basins (DeCelles and Giles, 1996). Such thrust faults can also be seen in Giambiagi et al. (2009) and Giambiagi et al. (2012) in their Figures 7b, 7c, and 2 (e.g., cross section H), respectively. Because the reverse faults beneath LPis x-1 are thought to be dipping to the west, identifying such faults below the TE-array (Figure 17a), but not below the TN-array (Figure 16a) is logical. Thus, we interpret the feature indicated by the dashed green line in Figure 17a as possibly corresponding to one of those deep thrusts.

The blue ellipses in Figure 17 indicate zones where dimmed-amplitude portions can be seen in the LEPC SI (Figure 17a) and global-phase SI results (Figure 17b). Because both independent methods use acoustic SI approaches, such dimming features might indicate weaker reflection responses in comparison with the other zones. Referring to the previous studies in this region, such weaker reflectivity might be due to the presence of the shallow asthenospheric plume that has been interpreted by Burd et al. (2014). Otherwise, such dimmed amplitudes might be indicative of partial-melting spots that are only locally present.

We also observe that the Moho in the LEPC SI results is not as visually dominant as the ones from the global-phase SI (Nishitsuji et al., 2016) and receiver-function method (Gilbert et al., 2006). This feature could be also found in other high-resolution reflection images by active-seismic sources. For instance, although the reflection results in Singh et al. (2006) and Calvert and McGeary (2013) provide a very fine scale of the images (e.g., 50 m in depth after Singh et al., 2006), we find that the Moho in their results is somewhat less prominent than in the image from seismic tomography (e.g., Calvert et al., 2011) and the receiver-function method (e.g., Gilbert et al., 2006). This is probably because the Moho discontinuity is rather better sensed with low frequencies (e.g., ≤ 1 Hz). The active-source reflection in Singh et al. (2006) and LEPC SI in this study used 10–30 and 1–5 Hz, respectively. The seismic tomography in Calvert et al. (2011) and the global-phase SI in Nishitsuji et al. (2016) used 0.03–0.3 and 0.3–1 Hz, respectively.

Therefore, as long as one's goal is the identification of the Moho, using the lower frequencies would in general be sufficient. Still, LEPC SI can provide useful information at a low acquisition cost when finer structural imaging and/or shallower targets are of interest (e.g., basin imaging if one can use higher frequency). For the current imaging resolution, LEPC SI could even assist in enhanced geothermal-system exploration together with magnetotelluric investigations. It is of importance for enhanced geothermal-system explorations to estimate the deeply lying conductive feature and the possible fault system between the thermal source (e.g., the Moho) and the target basement (up to 10 km). The success of the method depends on the illumination of the receiver array by the coda wavefield. In our case, the results show illumination directivity at the TE-array for the coda-waves part we use. The main advantage of the method is that it turns the passive recordings into reflection recordings, which is not possible without using SI. Note that active-source measurements in the frequency bandwidth we use in this study are not always available. In this case, LEPC SI might complement the low-frequency bandwidth and would be a useful alternative approach.

Conclusion

We presented SI for P-wave coda from local earthquakes (LEPC SI) to obtain crustal-scale reflection imaging without active sources. We applied LEPC SI with a linear array in the Malargüe region, Argentina, where a part of the Neuquén basin exists underneath. We compared SI by crosscorrelation, crosscoherence, and MDD, each followed by standard seismic processing from exploration seismology. For the MDD method, we found that the truncated SVD scheme gave a more stable solution of the matrix inversion than the one by damped least squares. This MDD result provided us with slightly better structural imaging at our scale of interest among all LEPC SI approaches we investigated. We also interpreted not only the deep thrust fault but also the possible melting zones that have been previously suggested by active-seismic (including exploration well) as well as magnetotelluric surveys. Depending on the frequency bandwidth, the availability of the local earthquakes, and the spatial sampling of receivers, LEPC SI has a potential to reveal not only the crustal-scale structure but also lithospheric- or basin-scale structures.

Acknowledgments

The data used in this study were collected using JWEED and IRIS (http://www.iris.edu/dms/nodes/dmc/). This research is supported by the Division for Earth and Life Sciences (ALW) with financial aid from the Netherlands Organization for Scientific Research (NWO) with grant VIDI 864.11.009. The research of K. Wapenaar was supported by the Netherlands Research Centre for Integrated Solid Earth Sciences. The authors thank IRIS-PASSCAL for providing the seismic equipment and the Argentine Ministry of Science, Technology and Production Innovation for the financial support connected to the transportation of the equipment. The authors also thank P. Auger Observatory and the Department of Civil Defense of Malargüe for the help during the data acquisition. The authors are thankful to C. Almagro Vidal, M. Holicki, J. van der Neut, I. Hartstra, and R. Charton at Delft University of Technology and I. Doi at Kyoto University for discussion. The authors are also grateful to N. Nakata, the associate editor, and four anonymous reviewers for their constructive comments that helped to improve the quality of this manuscript. Seismic analysis code (SAC2000) was used for a part of the data processing. The maps were drawn with GenericMappingTool (Wessel and Smith, 1991) and MATLAB.

APPENDIX A

Approximated multidimensional deconvolution

Here, we show the derivation to obtain the approximate expression for SI by approximated MDD — equation 5 in the main text. First, we define the following relation in the frequency domain ω:

$$\bar{v}_z(\mathbf{x}_B,\omega) = \bar{v}_z^d(\mathbf{x}_B,\omega) + \bar{v}_z^c(\mathbf{x}_B,\omega), \quad \text{(A-1)}$$

where $\bar{v}_z(\mathbf{x}_B,\omega)$ is the vertical component z of the particle velocity vector in the absence of a free surface at the receiver $\mathbf{x}_B$ for a local earthquake in the subsurface, $\bar{v}_z^d(\mathbf{x}_B,\omega)$ represents only the direct arrival, and $\bar{v}_z^c(\mathbf{x}_B,\omega)$ represents the coda, i.e., the scattering between inhomogeneities inside the medium. For the situation in which there is a free surface at the receiver level, we also define the following relation:

$$v_z(\mathbf{x}_B,\omega) = v_z^d(\mathbf{x}_B,\omega) + v_z^c(\mathbf{x}_B,\omega), \quad \text{(A-2)}$$

which is the free-surface counterpart of equation A-1. Note that $v_z^c(\mathbf{x}_B,\omega)$ is the coda wavefield we actually observe (see the light blue shades in Figure 6). Taking into account the fact that $v_z^d(\mathbf{x}_B,\omega) = 2\bar{v}_z^d(\mathbf{x}_B,\omega)$, equation A-2 can be rewritten as

$$v_z(\mathbf{x}_B,\omega) = 2\bar{v}_z^d(\mathbf{x}_B,\omega) + v_z^c(\mathbf{x}_B,\omega). \quad \text{(A-3)}$$

Using equations A-1 and A-3, we can write for the scattered field

$$\begin{aligned} v_z^{\text{scatt}}(\mathbf{x}_B,\omega) &= v_z(\mathbf{x}_B,\omega) - 2\bar{v}_z(\mathbf{x}_B,\omega) \\ &= v_z^c(\mathbf{x}_B,\omega) - 2\bar{v}_z^c(\mathbf{x}_B,\omega). \end{aligned} \quad \text{(A-4)}$$

Here, we recall equation 63 in Wapenaar et al. (2011)

$$v_z^{\text{scatt}}(\mathbf{x}_B,\omega) = A\iint_{\partial D_0} G_{z,z}^{\text{scatt}}(\mathbf{x}_B,\mathbf{x},\omega)\bar{v}_z(\mathbf{x},\omega)d^2\mathbf{x}, \quad \text{(A-5)}$$

where $G_{z,z}^{\text{scatt}}$ is the scattered Green's function and A is an amplitude-scaling factor due to the approximation that $\bar{v}_z(\mathbf{x},\omega)$ under the integral is proportional to the pressure measurement. The integral in equation A-5 is taken along the receiver positions (earth's surface ∂D_0). Substituting equations A-1 and A-4 into equation A-5, we get

$$\begin{aligned} v_z^c(\mathbf{x}_B,\omega) - 2\bar{v}_z^c(\mathbf{x}_B,\omega) = A\iint_{\partial D_0} & G_{z,z}^{\text{scatt}}(\mathbf{x}_B,\mathbf{x},\omega) \\ & \times\{\bar{v}_z^d(\mathbf{x},\omega) + \bar{v}_z^c(\mathbf{x},\omega)\}d^2\mathbf{x}. \end{aligned} \quad \text{(A-6)}$$

Multiplying equation A-6 with $\bar{v}_z^c(\mathbf{x}_A,\omega)^*$ and summation over the available sources, we get

$$\begin{aligned} &\sum_{S=1}^{n}[v_z^c(\mathbf{x}_B,\omega)\{\bar{v}_z^c(\mathbf{x}_A,\omega)\}^*] - 2\Gamma(\mathbf{x}_B,\mathbf{x}_A,\omega) \\ &= A\iint_{\partial D_0} G_{z,z}^{\text{scatt},d}(\mathbf{x}_B,\mathbf{x},\omega) \\ &\times\left[\sum_{S=1}^{n}[\bar{v}_z^d(\mathbf{x},\omega)\{\bar{v}_z^c(\mathbf{x}_A,\omega)\}^*] + \Gamma(\mathbf{x},\mathbf{x}_A,\omega)\right]d^2\mathbf{x}, \end{aligned} \quad \text{(A-7)}$$

where $*$ denotes the complex conjugate and Γ is the PSF (Wapenaar et al., 2011), defined as

$$\Gamma(\mathbf{x}_B,\mathbf{x}_A,\omega) = \sum_{S=1}^{n}[\bar{v}_z^c(\mathbf{x}_B,\omega)\{\bar{v}_z^c(\mathbf{x}_A,\omega)\}^*]. \quad \text{(A-8)}$$

Equation A-7 can be also written as

$$\begin{aligned} &\sum_{S=1}^{n}[v_z^c(\mathbf{x}_B,\omega)\{v_z^c(\mathbf{x}_A,\omega)\}^*] - 2\Gamma(\mathbf{x}_B,\mathbf{x}_A,\omega) \\ &+\sum_{S=1}^{n}[v_z^c(\mathbf{x}_B,\omega)[\{\bar{v}_z^c(\mathbf{x}_A,\omega) - v_z^c(\mathbf{x}_A,\omega)\}^*]] \\ &-A\iint_{\partial D_0} G_{z,z}^{\text{scatt},d}(\mathbf{x}_B,\mathbf{x},\omega)\sum_{S=1}^{n}[\bar{v}_z^d(\mathbf{x},\omega)\{\bar{v}_z^c(\mathbf{x}_A,\omega)\}^*]d^2\mathbf{x} \\ &= A\iint_{\partial D_0} G_{z,z}^{\text{scatt},d}(\mathbf{x}_B,\mathbf{x},\omega)\Gamma(\mathbf{x},\mathbf{x}_A,\omega)d^2\mathbf{x}. \end{aligned} \quad \text{(A-9)}$$

The third and fourth terms on the left side of equation A-9 retrieve events that are already retrieved by the first term on the left side. Thus, the third and fourth terms can be seen as amplitude corrections to the events retrieved by the first term. If we neglect them to obtain equation 5, we will not obtain correct amplitudes on the left side of equation A-9, and we will introduce artifacts. Still, the MDD of the first two terms on the left side by Γ will result in the compensation of the result retrieved from SI by crosscorrelation for inhomogeneous illumination. Furthermore, because Γ cannot be obtained directly, we approximate it by only the dominant arrivals in the result from SI by crosscorrelation (see, e.g., Figure 9c and 9f).

APPENDIX B

Truncated singular-value decomposition

In Figure B-1, we show the truncated singular values for the TN- and TE-arrays.

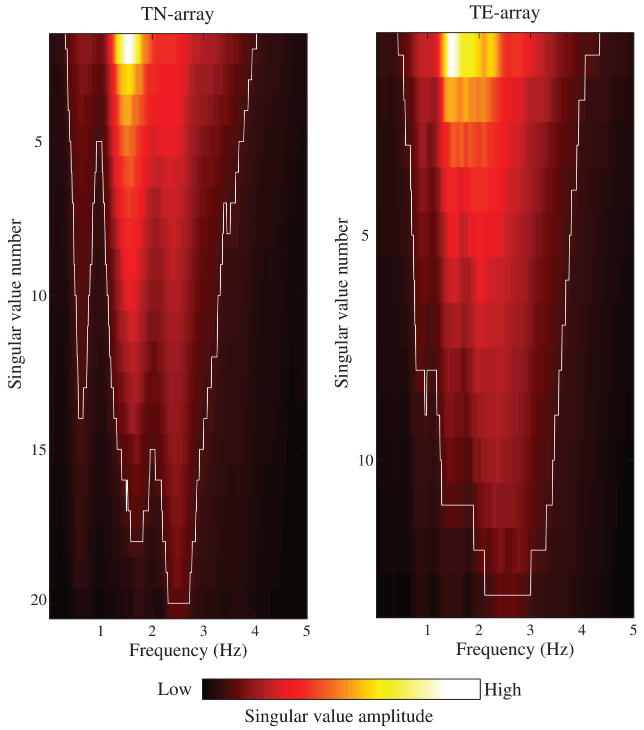

Figure B-1. Truncated singular values for the TN- and TE-arrays. The white lines show where 10% of the maximum singular value lie. We truncate the lower amplitude within the white line for MDD.

REFERENCES

Abe, S., E. Kurashimo, H. Sato, N. Hirata, T. Iwasaki, and T. Kawanaka, 2007, Interferometric seismic imaging of crustal structure using scattered teleseismic waves: Geophysical Research Letters, **34**, L19305, doi: 10.1029/2007GL030633.

Abercrombie, R., 2012, Comparison of direct and coda wave stress drop measurements for the Wells, Nevada, earthquake sequence: Journal of Geophysical Research, **118**, 1458–1470, doi: 10.1029/2012JB009638.

Aki, K., 1957, Space and time spectra of stationary waves with special reference to microtremors: Bulletin of the Earthquake Research Institute, University of Tokyo, **35**, 415–456.

Aki, K., A. Christoffersson, and E. S. Husebye, 1977, Determination of the three-dimensional seismic structure of the lithosphere: Journal of Geophysical Research, **82**, 277–296, doi: 10.1029/JB082i002p00277.

Almagro Vidal, C., D. Draganov, J. van der Neut, G. Drijkoningen, and K. Wapennar, 2014, Retrieval of reflections from ambient noise using illumination diagnosis: Geophysical Journal International, **198**, 1572–1584, doi: 10.1093/gji/ggu164.

Atkinson, G. M., and D. M. Boore, 1987, On the m_N, M relation for eastern North American earthquakes: Seismological Research Letters, **58**, 119–124, doi: 10.1785/gssrl.58.4.119.

Baltay, A., G. Prieto, and G. C. Beroza, 2010, Radiated seismic energy from coda measurements and no scaling in apparent stress with seismic moment: Journal of Geophysical Research, **115**, B08314, doi: 10.1029/2009JB006736.

Becker, J. J., D. T. Sandwell, W. H. F. Smith, J. Braud, B. Binder, J. Depner, D. Fabre, J. Factor, S. Ingalls, S. H. Kim, R. Ladner, K. Marks, S. Nelson, A. Pharaoh, R. Trimmer, J. Von Rosenberg, G. Wallace, and P. Weatherall, 2009, Global bathymetry and elevation data at 30 arc seconds resolution: SRTM30_PLUS: Marine Geodesy, **32**, 355–371, doi: 10.1080/01490410903297766.

Borko, H., and M. D. Bernick, 1963, Automatic document classification: Journal of the Association for Computing Machinery, **10**, 151–162, doi: 10.1145/321160.321165.

Boullenger, B., J. Hunziker, and D. Draganov, 2015, Reflection-response retrieval with seismic interferometry by multidimensional deconvolution from surface reflection data: 77th Annual International Conference and Exhibition, EAGE, Extended Abstracts, We N112 06, doi: 10.3997/2214-4609.201412981.

Burd, A. I., J. R. Booker, R. Mackie, A. Favetto, and M. C. Pomposiello, 2014, Three-dimensional electrical conductivity in the mantle beneath the Payún Matrú Volcanic Field in the Andean backarc of Argentina near 36.5°S: Evidence for decapitation of a mantle plume by resurgent upper mantle shear during slab steepening: Geophysical Journal International, **198**, 812–827, doi: 10.1093/gji/ggu145.

Calvert, A. J., and S. E. McGeary, 2013, Seismic reflection imaging of ultradeep roots beneath the eastern Aleutian island arc: Geology, **41**, 203–206, doi: 10.1130/G33683.1.

Calvert, A. J., L. A. Preston, and A. M. Farahbod, 2011, Sedimentary underplating at the Cascadia mantle-wedge corner revealed by seismic imaging: Nature Geoscience, **4**, 545–548, doi: 10.1038/ngeo1195.

Campillo, M., and A. Paul, 2003, Long-range correlations in the diffuse seismic coda: Science, **299**, 547–549, doi: 10.1126/science.1078551.

Claerbout, J., 1968, Synthesis of a layered medium from its acoustic transmission response: Geophysics, **33**, 264–269, doi: 10.1190/1.1439927.

DeCelles, P. G., and K. A. Giles, 1996, Foreland basin systems: Basin Research, **8**, 105–123, doi: 10.1046/j.1365-2117.1996.01491.x.

Doi, I., and H. Kawakata, 2013, High resolution spatial distribution of the velocity discontinuities in and around the swarm region beneath the Wakayama district, southwest Japan: Bulletin of the Seismological Society of America, **103**, 2135–2141, doi: 10.1785/0120120316.

Draganov, D., X. Campman, J. Thorbecke, A. Verdel, and K. Wapenaar, 2009, Reflection images from ambient seismic noise: Geophysics, **74**, no. 5, A63–A67, doi: 10.1190/1.3193529.

Duvall, T. L., Jr., S. M. Jefferies, J. W. Harvey, and M. A. Pomerantz, 1993, Time-distance helioseismology: Nature, **362**, 430–432, doi: 10.1038/362430a0.

Emoto, K., M. Campillo, F. Brenguier, X. Briand, and T. Takeda, 2015, Asymmetry of coda cross-correlation function: Dependence of the epicentre location: Geophysical Journal International, **201**, 1313–1323, doi: 10.1093/gji/ggv081.

Farías, M., D. Comte, R. Charrier, J. Martinod, C. David, A. Tassara, and A. Fock, 2010, Crustal-scale structural architecture in central Chile based on seismicity and surface geology: Implications for Andean mountain building: Tectonics, **29**, TC3006, doi: 10.1029/2009TC002480.

Garcia, D., 2010, Robust smoothing of gridded data in one and higher dimensions with missing values: Computational Statistics and Data Analysis, **54**, 1167–1178, doi: 10.1016/j.csda.2009.09.020.

Giambiagi, L., M. Ghiglione, E. Cristallini, and G. Bottesi, 2009, Kinematic models of basement/cover interaction: Insights from the Malargüe fold and thrust belt, Mendoza, Argentina: Journal of Structural Geology, **31**, 1443–1457, doi: 10.1016/j.jsg.2009.10.006.

Giambiagi, L., J. Mescua, F. Bechis, A. Tassara, and G. Hoke, 2012, Thrust belts of the southern Central Andes: Along-strike variations in shortening, topography, crustal geometry, and denudation: Geological Society of America Bulletin, **124**, 1339–1351, doi: 10.1130/B30609.1.

Gilbert, H., S. Beck, and G. Zandt, 2006, Lithospheric and upper mantle structure of central Chile and Argentina: Geophysical Journal International, **165**, 383–398, doi: 10.1111/j.1365-246X.2006.02867.x.

Granath, J. W., R. C. Whittaker, V. Singh, D. E. Bird, and M. G. Dinkelman, 2010, Full crustal seismic imaging in northeast Greenland: First Break, **28**, 79–83.

Golub, G. H., and C. F. van Loan, 1983, Matrix computations: The Johns Hopkins University Press.

Kanamori, H., and E. E. Brodsky, 2004, The physics of earthquakes: Reports on Progress in Physics, **67**, 1429–1496, doi: 10.1088/0034-4885/67/8/R03.

Kayal, J. R., 2008, Microearthquake seismology and seismotectonics of south Asia: Springer.

Kennett, B. L. N., E. R. Engdahl, and R. Buland, 1995, Constraints on seismic velocities in the earth from travel times: Geophysical Journal International, **122**, 108–124, doi: 10.1111/j.1365-246X.1995.tb03540.x.

Klema, V., and A. Laub, 1980, The singular value decomposition: Its computation and some applications: IEEE Transactions on Automatic Control, **25**, 164–176, doi: 10.1109/TAC.1980.1102314.

Kraemer, P., J. Silvestro, F. Achilli, and W. Brinkworth, 2011, Kinematics of a hybrid thick-thin-skinned fold and thrust belt recorded in Neogene syntectonic wedge-top basins, southern central Andes between 35° and 36°S, Malargüe, Argentina, *in* K. McClay, J. Shaw, and J. Suppe, eds., Thrust fault-related folding: AAPG Memoir 94, 245–270, doi: 10.1306/13251340M943099.

Langston, C. A., 1979, Structure under Mount Rainier, Washington, inferred from teleseismic body waves: Journal of Geophysical Research, **84**, 4749–4762, doi: 10.1029/JB084iB09p04749.

Mayeda, K., L. Malagnini, and W. R. Walter, 2007, A new spectral ratio method using narrow band coda envelopes: Evidence for non-self-similarity in the Hector Mine sequence: Geophysical Research Letters, **34**, L11303, doi: 10.1029/2007GL030041.

Menke, W., 1989, Geophysical data analysis: Discrete inverse theory: Academic Press.

Mescua, J. F., L. B. Giambiagi, and V. A. Ramos, 2013, Late Cretaceous uplift in the Malargüe fold-and-thrust belt (35°S), southern Central Andes of Argentina and Chile: Andean Geology, **40**, 102–116, doi: 10.5027/andgeoV40n1-a05.

Minato, S., T. Matsuoka, and T. Tsuji, 2013, Singular-value decomposition analysis of source illumination in seismic interferometry by multidimensional deconvolution: Geophysics, **78**, no. 3, Q25–Q34, doi: 10.1190/geo2012-0245.1.

Minato, S., T. Matsuoka, T. Tsuji, D. Draganov, J. Hunziker, and K. Wapenaar, 2011, Seismic interferometry using multidimensional deconvolution and crosscorrelation for crosswell seismic reflection data without borehole sources: Geophysics, **76**, no. 1, SA19–SA34, doi: 10.1190/1.3511357.

Nakahara, H., and M. M. Haney, 2015, Point spread functions for earthquake source imaging: An interpretation based on seismic interferometry: Geophysical Journal International, **202**, 54–61, doi: 10.1093/gji/ggv109.

Nakata, N., R. Snieder, and M. Behm, 2014, Body-wave interferometry using regional earthquakes with multidimensional deconvolution after wavefield decomposition at free surface: Geophysical Journal International, **199**, 1125–1137, doi: 10.1093/gji/ggu316.

Nakata, N., R. Snieder, T. Tsuji, K. Larner, and T. Matsuoka, 2011, Shear wave imaging from traffic noise using seismic interferometry by cross-coherence: Geophysics, **76**, no. 6, SA97–SA106, doi: 10.1190/geo2010-0188.1.

Nishitsuji, Y., E. Ruigrok, M. Gomez, and D. Draganov, 2014, Global-phase H/V spectral ratio for delineating the basin in the Malargüe region, Argentina: Seismological Research Letters, **85**, 1004–1011, doi: 10.1785/0220140054.

Nishitsuji, Y., E. Ruigrok, M. Gomez, K. Wapenaar, and D. Draganov, 2016, Reflection imaging of aseismic zone of the Nazca slab by global-phase seismic interferometry: Interpretation, 4, this issue, doi: 10.1190/int-2015-0225.1.

Operto, S., J. Virieux, J.-X. Dessa, and G. Pascal, 2006, Crustal seismic imaging from multifold ocean bottom seismometer data by frequency domain full waveform tomography: Application to the eastern Nankai trough: Journal of Geophysical Research, **111**, B09306, doi: 10.1029/2005JB003835.

Panea, I., D. Draganov, C. Almagro Vidal, and V. Mocanu, 2014, Retrieval of reflections from ambient noise recorded in the Mizil area, Romania: Geophysics, **79**, no. 3, Q31–Q42, doi: 10.1190/geo2013-0292.1.

Paul, A., M. Campillo, L. Margerin, and E. Larose, 2005, Empirical synthesis of time-asymmetrical Green functions from the correlation of coda waves: Journal of Geophysical Research, **110**, B08302, doi: 10.1029/2004JB003521.

Pearson, K., 1901, On lines and planes of closest fit to systems of points in space: Philosophical Magazine, **2**, 559–572, doi: 10.1080/14786440109462720.

Prieto, G. A., J. F. Lawrence, and G. C. Beroza, 2009, Anelastic earth structure from the coherency of the ambient seismic field: Journal of Geophysical Research, **114**, B07303, doi: 10.1029/2008JB006067.

Ruigrok, E., D. Draganov, M. Gomez, J. Ruzzante, D. Torres, I. Lopes Pumarega, N. Barbero, A. Ramires, A. R. Castano Ganan, K. van Wijk, and K. Wapenaar, 2012, Malargüe seismic array: Design and deployment for the temporary array: The European Physical Journal Plus, **127**, 126, doi: 10.1140/epjp/i2012-12126-7.

Ryberg, T., 2011, Body wave observations from cross-correlations of ambient seismic noise: A case study from the Karoo, RSA: Geophysical Research Letters, **38**, L13311, doi: 10.1029/2011GL047665.

Shapiro, N. M., and M. Campillo, 2004, Emergence of broadband Rayleigh waves from correlations of the ambient seismic noise: Geophysical Research Letters, **31**, L07614-1–L07614-4, doi: 10.1029/2004GL019491.

Singh, S. C., A. J. Harding, G. M. Kent, M. C. Sinha, V. Combier, S. Bazin, C. H. Tong, J. W. Pye, P. J. Barton, R. W. Hobbs, R. S. White, and J. A. Orcutt, 2006, Seismic reflection images of the Moho underlying melt sills at the East Pacific Rise: Nature, **442**, 287–290, doi: 10.1038/nature04939.

Slob, E., D. Draganov, and K. Wapenaar, 2007, Interferometric electromagnetic Green's functions representations using propagation invariants: Geophysical Journal International, **169**, 60–80, doi: 10.1111/j.1365-246X.2006.03296.x.

Snieder, R., 2004, Extracting the Green's function from the correlation of coda waves: A derivation based on stationary phase: Physical Review E, **69**, 046610, doi: 10.1103/PhysRevE.69.046610.

Snieder, R., and E. Şafak, 2006, Extracting the building response using seismic interferometry: Theory and application to the Millikan Library in Pasadena, California: Bulletin of the Seismological Society of America, **96**, 586–598, doi: 10.1785/0120050109.

Snieder, R., K. Wapenaar, and K. Larner, 2006, Spurious multiples in seismic interferometry of primaries: Geophysics, **71**, no. 4, SI111–SI124, doi: 10.1190/1.2211507.

van der Neut, J., E. Ruigrok, and K. Wapenaar, 2010, Retrieving the earth's reflection response by multidimensional deconvolution of ambient noise: 72nd Annual International Conference and Exhibition, EAGE, Extended Abstracts, P406, doi: 10.3997/2214-4609.201401259.

van der Neut, J., J. Thorbecke, K. Metha, E. Slob, and K. Wapenaar, 2011, Controlled-source interferometric redatuming by crosscorrelation and multidimensional deconvolution in elastic media: Geophysics, **76**, no. 4, SA63–SA76, doi: 10.1190/1.3580633.

Vasconcelos, I., and R. Snieder, 2008a, Interferometry by deconvolution: Part 1 — Theory for acoustic waves and numerical examples: Geophysics, **73**, no. 3, S115–S128, doi: 10.1190/1.2904554.

Vasconcelos, I., and R. Snieder, 2008b, Interferometry by deconvolution: Part 2 — Theory for elastic waves and application to drill-bit seismic imaging: Geophysics, **73**, no. 3, S129–S141, doi: 10.1190/1.2904985.

Wapenaar, K., 2004, Retrieving the elastodynamic Green's function of an arbitrary inhomogeneous medium by cross correlation: Physical Review Letters, **93**, 254–301, doi: 10.1103/PhysRevLett.93.254301.

Wapenaar, K., J. van der Neut, and E. Ruigrok, 2008, Passive seismic interferometry by multidimensional deconvolution: Geophysics, **73**, no. 6, A51–A56, doi: 10.1190/1.2976118.

Wapenaar, K., J. van der Neut, E. Ruigrok, D. Draganov, J. Hunziker, E. Slob, J. Thorbecke, and R. Snieder, 2011, Seismic interferometry by crosscorrelation and by multidimensional deconvolution: A systematic comparison: Geophysical Journal International, **185**, 1335–1364, doi: 10.1111/j.1365-246X.2011.05007.x.

Wessel, P., and W. H. F. Smith, 1991, Free software helps map and display data: EOS Transactions AGU, **72**, 441–448, doi: 10.1029/90EO00319.

Yilmaz, Ö., 1987, Seismic data analysis: SEG.

Zhan, Z., S. Ni, D. V. Helmberger, and R. W. Clayton, 2010, Retrieval of Moho-reflected shear wave arrivals from ambient seismic noise: Geophysical Journal International, **182**, 408–420, doi: 10.1111/j.1365-246X.2010.04625.x.

Zhao, J., Z. Jin, W. D. Mooney, N. Okaya, S. Wang, X. Gao, L. Tang, S. Pei, H. Liu, and Q. Xu, 2013, Crustal structure of the central Qaidam basin imaged by seismic wide-angle reflection/refraction profiling: Tectonophysics, **584**, 174–190, doi: 10.1016/j.tecto.2012.09.005.

Yohei Nishitsuji received an M.S. (2008) in geophysics from Kyoto University, Japan. He worked at Mitsui Oil Exploration Co. Ltd. for five years as a geophysicist. During this period, he worked on technical due diligence, seismic processing, and seismic interpretation for oil and gas assets. He then joined Delft University of Technology (TU Delft) in the Netherlands as a Ph.D. candidate. His project concentrates on cost-effective seismic investigations, including seismic interferometry. He is a member of SEG and EAGE.

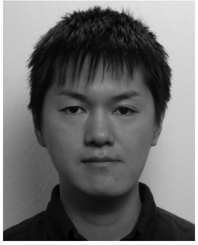

Shohei Minato received a Ph.D. (2012) in geophysics from Kyoto University, Japan. He then joined TU Delft as a postdoctoral research scientist, where he continues working with the innovative research of seismic interferometry, seismic imaging, and characterization. He is currently an associate editor for *Exploration Geophysics*. He is a member of SEG, EAGE, SEGJ, and EGU.

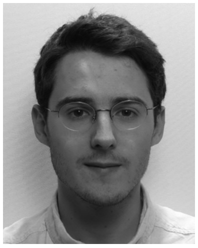

Boris Boullenger received an M.S. (2012) in applied geophysics from TU Delft. He is a graduate of École Centrale de Marseille. He is currently a Ph.D. candidate in applied geophysics at TU Delft, where his research interests include interferometric methods for seismic processing and imaging. He is a member of SEG and EAGE.

Martín Gomez received a Ph.D. (2012) in science and technology of materials from the Universidad de San Martin, Jorge Sabato Institute of Technology, Buenos Aires, Argentina. Since 2004, he has been an assistant professor at National Technologic University (UTN), Argentina. Also, he currently is the scientific director of the International Center of Earth Sciences, a Project belonging to the National Commission of Atomic Energy (CNEA), Buenos Aires, Argentina.

Kees Wapenaar received a Ph.D. (1986) in applied sciences from Delft University of Technology (TU Delft), the Netherlands. At TU Delft, he was associate professor in the Department of Applied Physics until 1999, when he was appointed the Antoni van Leeuwenhoek Professor in the Department of Geotechnology. Since 2002, he has been head of the applied geophysics and petrophysics section at that department. His research interests include wave theory and its applications in seismic imaging, multicomponent processing, and seismic interferometric methods. He received SEG's best paper in GEOPHYSICS award (2006), the Virgil Kauffman Gold Medal (2010), EAGE's Conrad Schlumberger award (2013), and he has served as editor-in-chief of GEOPHYSICS from 2007 until 2009. He is a member of SEG, EAGE, AGU, and ASA.

Deyan Draganov received an M.S. (1997) in geophysics from the University of Mining and Geology, Bulgaria, an M.S. (2002) in applied geophysics, and a Ph.D. (2007) in geophysics from TU Delft. Currently, he is assistant professor at TU Delft. Since 2005, he has been an associate editor for GEOPHYSICS. In 2010, he received the J. Clarence Karcher award from SEG. He is a member of SEG and EAGE.